IOP Publishing

Inverse Problems

Inverse Problems **38** (2022) 045010 (28pp)

https://doi.org/10.1088/1361-6420/ac5525

Polarimetric radar interferometry in the presence of differential Faraday rotation

Mikhail Gilman* and **Semyon Tsynkov**

Department of Mathematics, North Carolina State University, Raleigh, NC 27695, United States of America

E-mail: mgilman@ncsu.edu, tsynkov@math.ncsu.edu, https://mgilman.math.ncsu.edu and https://stsynkov.math.ncsu.edu

Received 7 October 2021, revised 11 February 2022
Accepted for publication 15 February 2022
Published 11 March 2022

Abstract

Faraday rotation (FR) affects the low-frequency transionospheric radar by creating cross-talk between polarizations. The baseline part of FR can be compensated for by applying an appropriate linear transformation—rotation with a known FR angle. Yet the differential Faraday rotation (dFR), which is a frequency-dependent part of FR, persists and introduces distortions into the observations. We build a simplified model with two polarimetric scattering channels that allows us to evaluate the effect of dFR on the accuracy of PolInSAR reconstruction. We also assess the severity of distortions due to dFR for the future BIOMASS mission and several other spaceborne radar systems.

Keywords: synthetic aperture radar, ionosphere, differential Faraday rotation, polarimetric radar interferometry

(Some figures may appear in colour only in the online journal)

1. Introduction

Standard synthetic aperture radar (SAR) imaging produces two-dimensional maps of the target reflectivity. The lack of a third dimension is due to the imaging geometry with an aperture that typically is a segment of a straight line (see, e.g., [1–3]). When the reflectivity function of a target is three-dimensional, the standard SAR collapses this function across the slant plane, which is a plane passing through the target and the aperture. Yet, 2D images yield a satisfactory representation of the geometric features of a scatterer that is flat or nearly flat, e.g., a patch of the Earth's surface. The literature on SAR is vast and includes many well-known sources, e.g., [3–8]. Among the more mathematical publications that may, in particular, make use of microlocal analysis, we mention [9–15] in addition to [3].

*Author to whom any correspondence should be addressed.

© 2022 IOP Publishing Ltd Printed in the UK

Interferometric SAR, or InSAR, is a first step towards obtaining a third coordinate in the radar image. For a scatterer that is two-dimensional but not flat, InSAR can supplement SAR by providing an elevation map [1, 2]. This is achieved by combining the complex-valued SAR images obtained from two apertures that correspond to two different slant planes and analyzing the phase difference between these images. Most often, InSAR involves apertures that are parallel or almost parallel, yielding two slightly different incident angles. Such technology has been used to build global digital elevation maps (DEMs) in satellite-based radar missions such as SRTM [16] and TanDEM-X [17]. A mathematical perspective on SAR interferometry is presented in our recent paper [18].

The need to extend the SAR imaging capacity to essentially three-dimensional targets, e.g., a vegetation-covered terrain, gave rise to more sophisticated technologies. In some experiments, more than 10 apertures were combined [19] to resolve details in the direction across the slant plane. Such setups are rare and expensive. By contrast, polarimetric radar interferometry (PolInSAR) [20–22] can extract multiple parameters of a three-dimensional scatterer using one pair of apertures. For example, by exploiting the difference in reflectivities and correlation properties between the ground and vegetation at different polarizations, PolInSAR retrieves the ground topography and average height and thickness of the vegetation layer covering the Earth's surface (modeled as a scattering volume above the ground).

Any cross-talk between the polarimetric channels of a radar system violates the PolInSAR assumptions and reduces its reconstruction accuracy. Differential Faraday rotation (dFR) in the Earth's ionosphere, see [23, 24], has been shown to be a potential source of such cross-talk for satellite-based radar systems. This effect is very small for the previously mentioned C/X-band SRTM and TanDEM-X missions because of their relatively high carrier frequency. However, the need for ground and foliage penetration necessitates the use of the radar systems with a much lower frequency. For example, the central frequency of the future BIOMASS radar [25, 26] is many times lower than those used in the past global radar DEM missions. It then makes sense to estimate the effect of dFR on both currently active and future systems.

Faraday rotation (FR) is rotation of the polarization plane of a linearly polarized electromagnetic signal propagating in a magnetized plasma, such as the Earth's ionosphere. Its effect on spaceborne SAR imaging has been studied by many authors [27–34]. In particular, FR can help obtain the total electron content (TEC) in the ionosphere, which is the electron concentration integrated in the vertical direction. In turn, dFR is due to the dependence of the FR angle on the frequency. Hence, for a pulsed radar with a certain bandwidth, dFR will always be present. The effect of dFR on the 'plain' polarimetric SAR has been analyzed in [23, 24, 35, 36], and a mitigation method for this effect, called the polarimetric matched filter (PMF), has been proposed in [23].[1] On the other hand, to the best of our knowledge the effect of dFR on polarimetric SAR interferometry has not been studied previously.

In this work, we assess the effect of dFR on PolInSAR reconstruction with no PMF mitigation. We operate in a simplified setting that uses only two polarimetric scattering channels but still captures the most significant features of a popular PolInSAR reflectivity model called random volume over ground (RVoG) [21]. Our formulation also includes additive noise and allows for the exact reconstruction of the parameters of interest—ground elevation and height and thickness of the scattering volume above ground (e.g., vegetation layer)—in the case where there is no dFR. When the same reconstruction procedure is applied to the simulated data that

[1] As opposed to interferometric SAR, plain SAR does not combine multiple (complex-valued) images for the purpose of deriving and using their phase difference.

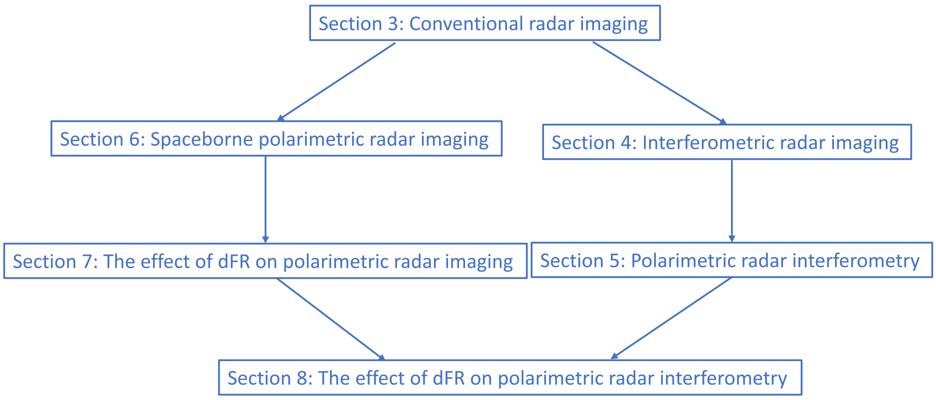

Figure 1. Organization of sections 3–7 that provide the background material for section 8.

are subject to dFR, discrepancies are observed between the reconstruction outcome and original parameters used for generating the data. These discrepancies yield a quantitative measure of the effect of dFR on PolInSAR reconstruction. The rationale behind this approach is the same as the one we have used previously for assessing the effect of ionospheric dispersion on conventional SAR imaging [37–39]—consider the data subject to dispersion, apply the reconstruction that does not take the dispersion into account, and quantify the resulting discrepancies.

In section 2, we summarize the most important new findings of the current work. In sections 3–7, we review the necessary background, namely, the conventional SAR imaging, radar interferometry (InSAR), PolInSAR, spaceborne polarimetric SAR (with no interferometry), and the effect of dFR on the latter, see figure 1. Section 8.1 defines a simplified RVoG model that is subsequently used for the analysis of PolInSAR reconstruction. In section 8.2, we consider a reduced noiseless formulation. In section 8.3, we introduce a PolInSAR reconstruction for the case with noise and no dFR. In section 8.4, we apply the reconstruction from section 8.3 to the simulated data with dFR, and evaluate the resulting discrepancies (errors) numerically. The discussion in section 9 shows where the proposed approach can be refined, and section 10 provides the conclusions.

A note about the terminology is in order. The significance of synthetic aperture in SAR imaging is that it provides the azimuthal resolution (along the track). At the same time, the analysis of both plain and PolInSAR is usually conducted in the cross-track plane. In this work, we do not consider the effects due to the synthetic aperture. For this reason, we use the term ‘radar interferometry’ instead of more common abbreviations InSAR and PolInSAR whenever this would not lead to misunderstanding.

2. Summary of findings

We have developed a quantitative methodology for estimating the effect of dFR on PolInSAR in spaceborne imaging. Our methodology involves a simplified RVoG model and an analytic approach to its inversion. The key factors that determine the magnitude of the said effect can be partitioned into several groups:

- Radar system parameters: carrier frequency and bandwidth (section 3 and appendix A).
- Geophysical parameters: Earth’s magnetic field and electron density in the ionosphere (section 6).

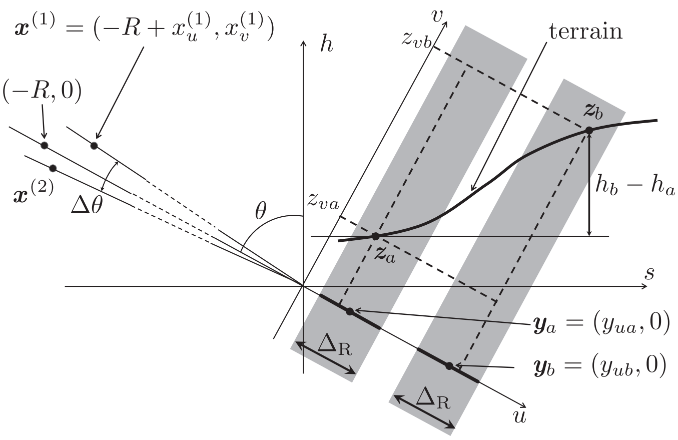

Figure 2. Schematic for radar imaging and interferometry. Annuli of width $\Delta_{\mathrm{R}} = \pi c/B$, see (5), represented by the bands centered about y_{ua} and y_{yb} are highlighted. All focusing locations, e.g., $\boldsymbol{y}_a$ or $\boldsymbol{y}_b$, are on the reference slant line between the satellite and the origin.

- Interferometric parameters: angle $\Delta\theta$ and wavenumber κ (section 4).
- Properties of the imaged terrain: ground topography, height and thickness of the scattering volume above the ground, ratios of scatterer reflectivities in different polarimetric channels, and the level of noise (sections 5 and 8).

Our analysis shows that the effect of dFR on PolInSAR reconstruction for the existing high frequency spaceborne SAR systems (X-, C-, and L-band) is negligible. For the contemplated P-band BIOMASS system (a lower carrier frequency) this effect is also small, but more borderline. For the future spaceborne SAR systems that may operate on low frequencies, the effect of dFR may be stronger and the need for developing and implementing the appropriate corrections will have to be evaluated in each specific case.

3. Conventional radar imaging

The exposition of all radar modalities in the current work is done in the cross-track plane, as common for interferometry (see the note at the end of section 1). Accordingly, all spatial coordinates are considered two-dimensional—one horizontal coordinate s (ground range) and one vertical coordinate h (elevation). For convenience of presentation, we will also be using the slanted coordinates (u, v) (see figure 2). A full physical setting would also involve a third coordinate, along-the-track or azimuthal, and the synthesis of aperture along this coordinate, that we do not consider hereafter. Note also that spatial dimensions other than 2 or 3 present no practical interest and are therefore not discussed in the radar literature.

Following [39, chapter 2], we specify the SAR interrogating signal as a narrow-band linear chirp (frequency modulated signal) with the carrier frequency ω_0, bandwidth B, duration τ, and rate $\alpha = B/2\tau > 0$ (see appendix A). We also assume that scattering at the target is weak and employ the first Born approximation[2]. Then, the SAR image $I = I(\boldsymbol{y})$ is given by convolution

[2] Conventional SAR reconstruction requires linearity with respect to the unknown ground reflectivity. A model for linearized scattering that is not necessarily weak is proposed in [40], see also [39, chapter 7].

of the unknown ground reflectivity $\nu = \nu(z)$ with the imaging kernel W:

$$I(\boldsymbol{y}) = \int W(R_{\boldsymbol{y}} - R_{\boldsymbol{z}})\nu(\boldsymbol{z})\mathrm{d}\boldsymbol{z}, \tag{1}$$

where $\boldsymbol{z} \in \mathbb{R}^2$ is the location in the target region, $\boldsymbol{y} \in \mathbb{R}^2$ is the focusing location, and $R_{\boldsymbol{z}}$ and $R_{\boldsymbol{y}}$ are the signal travel distances between those respective locations and the spaceborne SAR antenna. In figure 2, the location of the antenna can be associated with either $\boldsymbol{x}^{(1)}$ or $\boldsymbol{x}^{(2)}$. The kernel W in (1) is known as the point spread function:

$$W(R_{\boldsymbol{y}} - R_{\boldsymbol{z}}) = \mathrm{e}^{-2\mathrm{i}k(R_{\boldsymbol{y}} - R_{\boldsymbol{z}})}\tau \,\mathrm{sinc}\left(\frac{B(R_{\boldsymbol{y}} - R_{\boldsymbol{z}})}{c}\right), \tag{2}$$

where $k = \omega_0/c$, c is the speed of light, and $\mathrm{sinc}\,\xi = \sin\xi/\xi$. The integration in (1) is performed over the entire space $\mathbb{R}^2$. Therefore, no integration limits are specified.

A point scatterer of strength ν_0 at the location $\boldsymbol{z}$ is given by a singular reflectivity:

$$\nu(\boldsymbol{z}') = \nu_0\delta(\boldsymbol{z}' - \boldsymbol{z}), \tag{3}$$

where $\delta(\cdot)$ is the Dirac delta function[3]. The image (1) of the point scatterer (3) is

$$I(\boldsymbol{y}) = \nu_0 \cdot \tau \,\exp[-2\mathrm{i}\omega_0(R_{\boldsymbol{y}} - R_{\boldsymbol{z}})/c]\mathrm{sinc}\left(B\frac{R_{\boldsymbol{y}} - R_{\boldsymbol{z}}}{c}\right). \tag{4}$$

In the two-dimensional coordinate space $\boldsymbol{z}$ (one horizontal and one vertical coordinate, see figure 2), the main lobe of the sinc function in (4) specifies an annulus of central radius $R_{\boldsymbol{y}}$ and thickness

$$\Delta_{\mathrm{R}} = \frac{\pi c}{B}. \tag{5}$$

In the SAR literature, the quantity Δ_{R} given by (5) is called the range resolution. It provides a key spatial scale for the analysis of SAR imaging. This scale is fully determined by the properties of the imaging system (specifically, the bandwidth B of the interrogating waveform) and is not related to the properties of the target.

The absolute value $|I(\boldsymbol{y})|$ of the function (4) has a single maximum at $R_{\boldsymbol{y}} = R_{\boldsymbol{z}}$. However, locating it with the accuracy much better than Δ_{R} is considered problematic in practical situations where the contributions from other scatterers, as well as noise, are present. As the radius of the annulus given by the main lobe of the sinc in (4) is very large, in the vicinity of the target it can be replaced with a band of width $\sim\Delta_{\mathrm{R}}$, as in figure 2. SAR imaging with kernel (2) cannot tell between different targets within such a band.

While the function $I = I(\boldsymbol{y})$ defined by (1) is a function of two arguments, $\boldsymbol{y} \in \mathbb{R}^2$, a conventional SAR image in the cross-track plane is interpreted as one-dimensional. Indeed, as the radar does not distinguish between the targets within a given grey band shown in figure 2, all those targets are collapsed onto one slant reference line $v = 0$. Hence, all focusing locations, such as $\boldsymbol{y}_a$ or $\boldsymbol{y}_b$ in figure 2, belong to this line, i.e., $y_{va} = 0$ and $y_{vb} = 0$.

[3] The assumption of weak scattering does not hold for the reflectivity function (3). A justification for the use of singular reflectivity (3) is given in [18, sections 3.3 and 3.4].

4. Radar interferometry

Consider the reflectivity $\nu(\boldsymbol{z})$ in the form of a Gaussian white noise [6]:

$$\langle\overline{\nu(\boldsymbol{z}')}\nu(\boldsymbol{z})\rangle = \sigma^2(\boldsymbol{z})\delta(\boldsymbol{z}'-\boldsymbol{z}), \tag{6}$$

where $\langle\ldots\rangle$ denotes statistical averaging. In practice, it is replaced with spatial averaging over a patch of terrain where σ^2 varies insignificantly and can be considered constant.

Assumption. Hereafter, we will be assuming that the size Δ_{P} of the averaging patch where $\sigma^2 \approx$ const is much larger than the resolution scale Δ_{R} given by (5): $\Delta_{\mathrm{P}} \gg \Delta_{\mathrm{R}}$.

The foregoing assumption is not guaranteed automatically, as the two scales are unrelated: Δ_{R} is determined by the imaging system and Δ_{P} is a characteristic of the target. The separation of scales $\Delta_{\mathrm{P}} \gg \Delta_{\mathrm{R}}$ is rather an independent requirement for the chosen mathematical model to be applicable. In many practical scenarios it holds.

Radar interferometry involves two antenna locations as shown in figure 2: $\boldsymbol{x}^{(1,2)} = (-R + x_u^{(1,2)}, x_v^{(1,2)})$. They define the interferometric angle $\Delta\theta$:

$$\theta_1 \approx \theta - \frac{x_v^{(1)}}{R}, \qquad \theta_2 \approx \theta - \frac{x_v^{(2)}}{R}, \qquad \Delta\theta = \theta_1 - \theta_2. \tag{7}$$

To reconstruct the scatterer elevation, we build a complex-valued interferogram as in [18]. For the image $I(\boldsymbol{y}) \equiv I(\boldsymbol{y};\ \boldsymbol{x}, \omega_0, B)$, we first introduce its alternative form:

$$\mathcal{I}(\boldsymbol{y};\boldsymbol{x},\omega_0,B) = I(\boldsymbol{y};\boldsymbol{x},\omega_0,B)\exp(2\mathrm{i}\omega_0 R_{\boldsymbol{y}}/c)$$

needed to eliminate the fast phase $\exp(-2\mathrm{i}\omega_0 R_{\boldsymbol{y}}/c)$. As in section 3, all focusing locations satisfy $y_v = 0$ (see figure 2). Then, the interferogram is formed according to

$$Q(\boldsymbol{y}) \equiv Q(\boldsymbol{y};\boldsymbol{x}^{(1)},\boldsymbol{x}^{(2)},\omega_1,\omega_2,\tilde{B}) \stackrel{\text{def}}{=} \left\langle \overline{\mathcal{I}(\boldsymbol{y}^{(1)};\boldsymbol{x}^{(1)},\omega_1,\tilde{B})}\mathcal{I}(\boldsymbol{y}^{(2)};\boldsymbol{x}^{(2)},\omega_2,\tilde{B})\right\rangle, \tag{8}$$

where the images from the two antennas must be co-registered [41] so that

$$|\boldsymbol{y}^{(1)} - \boldsymbol{y}| \ll \Delta_{\mathrm{R}}, \qquad |\boldsymbol{y}^{(2)} - \boldsymbol{y}| \ll \Delta_{\mathrm{R}}.$$

As in (6), statistical averaging $\langle\ldots\rangle$ on the right-hand side of (8) is replaced with spatial averaging over a region of size Δ_{P}. The central frequencies ω_1, ω_2 and bandwidth $\tilde{B}$ of the sub-bands in (8) are chosen as

$$\frac{\omega_1}{c} = k_1 = k - \frac{\Delta k}{2}, \qquad \frac{\omega_2}{c} = k_2 = k + \frac{\Delta k}{2}, \qquad \tilde{B} = B - |\Delta k|c, \tag{9}$$

where $\Delta k = k\frac{\Delta\theta}{\tan\theta}$ and $\Delta\theta = \theta_1 - \theta_2$ is the interferometric angle defined in (7), $|\Delta\theta| \ll 1$. This choice of sub-bands is called the wavenumber adjustment or range spectral filtering [18].

For the imaging kernel (2), scatterer (6), and interferometric parameters satisfying (9), the interferogram (8) can be expressed as follows [18]:

$$Q(\boldsymbol{y}) = \exp(\mathrm{i}\Phi_Q)\left(\frac{\tau\tilde{B}}{B}\right)^2 \int \exp[-\mathrm{i}\kappa h(\boldsymbol{z})]\mathrm{sinc}^2\left(\frac{\tilde{B}(R_{\boldsymbol{y}} - R_{\boldsymbol{z}})}{c}\right)\sigma^2(\boldsymbol{z})\mathrm{d}\boldsymbol{z}, \tag{10}$$

where κ is called the interferometric wavenumber:

$$\kappa = 2k\frac{\Delta\theta}{\sin\,\theta}, \tag{11}$$

and $h(\boldsymbol{z})$ is the elevation of the point $\boldsymbol{z}$ above the horizontal plane $h = 0$ (see figure 2). The quantity Φ_Q in (10) is the common interferometric phase:

$$\Phi_Q = 2k\left(-\left(x_u^{(2)} - x_u^{(1)}\right) + \frac{\left(x_v^{(2)}\right)^2 - \left(x_v^{(1)}\right)^2}{2R}\right) + \Delta k(2R - x_u^{(1)} - x_u^{(2)}). \tag{12}$$

The key role of the wavenumber adjustment (9) is that it has eliminated the dependence of the interferometric phase in the integrand of (10) on the horizontal coordinate [18, 42, 43].

The uncertainties in the platform positions, most importantly—$x_u^{(1)}$ and $x_u^{(2)}$ on the right-hand side of (12), may easily exceed the radar wavelength, yielding the absolute error values of Φ_Q significantly larger than π [18]. Nonetheless, in the following procedure the unknown common phase Φ_Q cancels, allowing one to retrieve the relative scatterer elevation.

Let $\boldsymbol{z}_a$ and $\boldsymbol{z}_b$ be two points on the scattering surface (see figure 2) that are farther apart from one another than Δ_{P} and suppose that the terrain elevation is (nearly) constant in the vicinity of each of these points so that we approximately have:

$$\sigma^2(\boldsymbol{z}) = \sigma_a^2\delta(h(\boldsymbol{z}) - h_a) \quad \text{and} \quad \sigma^2(\boldsymbol{z}) = \sigma_b^2\delta(h(\boldsymbol{z}) - h_b). \tag{13}$$

Then, we obtain from (10):

$$\frac{Q(\boldsymbol{y}_b)}{Q(\boldsymbol{y}_a)} = \frac{\sigma_b^2}{\sigma_a^2}\,\exp[-\mathrm{i}\kappa(h_b - h_a)]. \tag{14}$$

Consequently, the elevation difference between the focusing locations $\boldsymbol{y}_a$ and $\boldsymbol{y}_b$ is

$$h_b - h_a = -\frac{\angle\left(Q(\boldsymbol{y}_b)/Q(\boldsymbol{y}_a)\right)}{\kappa},$$

where $\angle$ is the argument of a complex number (complex phase). As $0 \leqslant \left|\angle\left(Q(\boldsymbol{y}_b)/Q(\boldsymbol{y}_a)\right)\right| < \pi$, the reconstructed height difference may not exceed a certain threshold:

$$|h_b - h_a| < \pi\frac{\sin\,\theta}{2k\Delta\theta} = \frac{\lambda\,\sin\,\theta}{4\Delta\theta} \tag{15}$$

equal to one half of the ambiguity height (i.e., a change in elevation that changes the interferometric phase by 2π, see, e.g., [44, 45]). In practice, elevations larger than the threshold (15) are reconstructed using the technique of phase unwrapping, see, e.g., [4, 7, 46]. Hereafter, we will assume that condition (15) and its equivalents are always met.

5. Polarimetric radar interferometry

PolInSAR seeks to reconstruct the dependence of $\sigma^2(\boldsymbol{z})$ on h from the values of the interferogram $Q(\boldsymbol{y})$ of (8) at different polarizations. Consider

$$\sigma^2(\boldsymbol{z}) \equiv \sigma^2(z_u, h(\boldsymbol{z})), \tag{16}$$

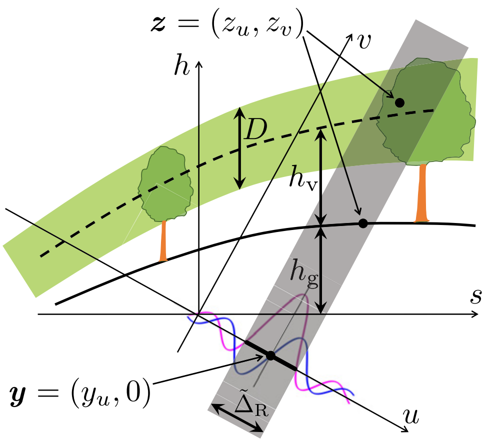

Figure 3. Geometric parameters of ground topography and vegetation layer in the RVoG model as given by (21). A band of width $\tilde{\Delta}_{\rm R} = \pi c/\tilde{B}$ is highlighted ($\tilde{B}$ is defined in (9)). For all scatterer coordinates $\boldsymbol{z}$ within this band, we use the same value of the interferogram $Q(\boldsymbol{y}) \equiv Q(y_u)$. The purple and blue curves illustrate $F_0(\xi;\ \eta)$ and $\eta^{-1}F_1(\xi;\ \eta)$, respectively, see (41), for small η and $\xi = \tilde{B}(y_u - z_u)/c$.

where σ^2 varies slowly on the sale of $\Delta_{\rm P}$ as a function of z_u. Yet $\mathrm{sinc}^2\left(\frac{\tilde{B}(R_{\boldsymbol{y}}-R_{\boldsymbol{z}})}{c}\right)$ under the integral (10) varies on the scale of $\tilde{\Delta}_{\rm R} = \pi c/\tilde{B} \sim \Delta_{\rm R}$ and over the distance $\Delta_{\rm P} \gg \Delta_{\rm R}$ it decays substantially. Therefore, for the coherence (10) we have (see [2] or [18] for detail):

$$Q(\boldsymbol{y}) \approx \exp(\mathrm{i}\Phi_Q)V_Q \int \exp(-\mathrm{i}\kappa h)\sigma^2(y_u, h)\mathrm{d}h, \tag{17}$$

where

$$V_Q = \left(\frac{\tau\tilde{B}}{B}\right)^2 \int \mathrm{sinc}^2\left(\frac{\tilde{B}s\,\sin\,\theta}{c}\right)\mathrm{d}s. \tag{18}$$

To reconstruct the dependence of $\sigma^2(y_u, h)$ on h for a given y_u, PolInSAR uses a parameterized form of $\sigma^2(y_u, h)$ and exploits the measurements of Q on multiple polarizations traditionally denoted by $\mathbf{w}$, so that the data are $Q(\boldsymbol{y}, \mathbf{w})$.[4] The most popular PolInSAR model, called RVoG [21], includes two statistically independent terms that represent the ground and volume (i.e., foliage) scatterers:

$$\nu(\boldsymbol{z}, \mathbf{w}) = \nu_{\rm Gr}(\boldsymbol{z}, \mathbf{w}) + \nu_{\rm Vol}(\boldsymbol{z}, \mathbf{w}), \quad \langle\overline{\nu_{\rm Gr}(\boldsymbol{z}, \mathbf{w})}\nu_{\rm Vol}(\boldsymbol{z}, \mathbf{w})\rangle = 0. \tag{19}$$

Additionally, we assume that $\nu_{\rm Gr}$ and $\nu_{\rm Vol}$ in (19) individually satisfy (6) and (16):

$$\begin{aligned}\langle\overline{\nu_{\rm Gr}(\boldsymbol{z}', \mathbf{w})}\nu_{\rm Gr}(\boldsymbol{z}, \mathbf{w})\rangle &= \sigma^2_{\rm Gr}(\boldsymbol{z}, \mathbf{w})\delta(z'_u - z_u)\delta\left(h(z'_u) - h(z_u)\right), \\ \langle\overline{\nu_{\rm Vol}(\boldsymbol{z}', \mathbf{w})}\nu_{\rm Vol}(\boldsymbol{z}, \mathbf{w})\rangle &= \sigma^2_{\rm Vol}(\boldsymbol{z}, \mathbf{w})\delta(z'_u - z_u)\delta\left(h(z'_u) - h(z_u)\right),\end{aligned} \tag{20}$$

[4] In this section, polarization $\mathbf{w}$ is interpreted as merely an additional variable that both the reflectivity and image depend on. A more physics-aware treatment of polarization is given in section 6.

and consider the following parametrization of the dependence of σ^2_{Gr} and σ^2_{Vol} in (20) on h:

$$\begin{aligned}\sigma^2_{\mathrm{Gr}}(\boldsymbol{z},\mathbf{w}) &= \sigma^2_{\mathrm{g}}(z_u,\mathbf{w})\delta\left(h-h_{\mathrm{g}}\right),\\ \sigma^2_{\mathrm{Vol}}(\boldsymbol{z},\mathbf{w}) &= \sigma^2_{\mathrm{v}}(z_u,\mathbf{w})\frac{1}{D}\chi_D\left(h-h_{\mathrm{g}}-h_{\mathrm{v}}\right).\end{aligned} \tag{21}$$

In formulae (21), $h_{\mathrm{g}}=h_{\mathrm{g}}(z_u)$ describes the ground topography, $h_{\mathrm{v}}=h_{\mathrm{v}}(z_u)$ and $D=D(z_u)$ denote the local elevation and thickness of the volume scatterer (foliage layer), see figure 3, and the characteristic function χ_D of the interval $[-D/2,D/2]$ is defined as follows:

$$\chi_D(h)=\begin{cases}1, & h\in[-D/2,D/2],\\ 0 & \text{otherwise}.\end{cases}$$

On a neighborhood of y_u of size Δ_{P}, we drop the dependence of D, h_{g}, h_{v}, σ^2_{g}, and σ^2_{v} on z_u as those quantities can be considered constant. We also drop the argument $\boldsymbol{y}$ from $Q(\boldsymbol{y},\mathbf{w})$ and ignore the difference between y_u and z_u because $|y_u-z_u|\lesssim\tilde{\Delta}_{\mathrm{R}}\ll\Delta_{\mathrm{P}}$. PolInSAR aims to retrieve h_{v}, D, and h_{g} near y_u from the measurements of $Q(\mathbf{w})$ for several different $\mathbf{w}$.

Let $\mathcal{I}_{\mathrm{Gr}}(\mathbf{w})$ and $\mathcal{I}_{\mathrm{Vol}}(\mathbf{w})$ be the image components due to ν_{Gr} and ν_{Vol}, respectively:

$$\mathcal{I}(\mathbf{w})=\mathcal{I}_{\mathrm{Gr}}(\mathbf{w})+\mathcal{I}_{\mathrm{Vol}}(\mathbf{w}). \tag{22}$$

Then, (19) implies that $Q(\mathbf{w})=Q_{\mathrm{Gr}}(\mathbf{w})+Q_{\mathrm{Vol}}(\mathbf{w})$, where, similar to (8),

$$\begin{aligned}Q_{\mathrm{Gr}}(\mathbf{w}) &= \left\langle\overline{\mathcal{I}_{\mathrm{Gr}}(\mathbf{w};\boldsymbol{x}^{(1)},\ldots)}\mathcal{I}_{\mathrm{Gr}}(\mathbf{w};\boldsymbol{x}^{(2)},\ldots)\right\rangle,\\ Q_{\mathrm{Vol}}(\mathbf{w}) &= \left\langle\overline{\mathcal{I}_{\mathrm{Vol}}(\mathbf{w};\boldsymbol{x}^{(1)},\ldots)}\mathcal{I}_{\mathrm{Vol}}(\mathbf{w};\boldsymbol{x}^{(2)},\ldots)\right\rangle.\end{aligned}$$

Next, we introduce the image intensities

$$T^{(1)}(\mathbf{w})=\left\langle\left|\mathcal{I}(\mathbf{w};\boldsymbol{x}^{(1)},k_1,\tilde{B})\right|^2\right\rangle,\qquad T^{(2)}(\mathbf{w})=\left\langle\left|\mathcal{I}(\mathbf{w};\boldsymbol{x}^{(2)},k_2,\tilde{B})\right|^2\right\rangle, \tag{23}$$

and assume that $T^{(1)}(\mathbf{w})\approx T^{(2)}(\mathbf{w})=T(\mathbf{w})$, because the imaging conditions for the two antennas are basically equivalent. Similarly to (17), one can derive:

$$T(\mathbf{w})=V_Q\int\sigma^2(h)\mathrm{d}h. \tag{24}$$

The total coherence and coherences of individual image components are defined as follows:

$$\gamma(\mathbf{w})=\frac{Q(\mathbf{w})}{T(\mathbf{w})},\qquad\gamma_{\mathrm{Gr}}(\mathbf{w})=\frac{Q_{\mathrm{Gr}}(\mathbf{w})}{T_{\mathrm{Gr}}(\mathbf{w})},\qquad\gamma_{\mathrm{Vol}}(\mathbf{w})=\frac{Q_{\mathrm{Vol}}(\mathbf{w})}{T_{\mathrm{Vol}}(\mathbf{w})}. \tag{25}$$

Substituting (21) into (17) and (24) and changing the variable: $h'=h-h_{\mathrm{g}}$, we can explicitly calculate the individual coherences in (25):

$$\gamma_{\mathrm{Gr}}=\exp[\mathrm{i}(\Phi_Q-\kappa h_{\mathrm{g}})]\gamma_{\mathrm{g}},\quad\text{where }\gamma_{\mathrm{g}}=\int\exp(-\mathrm{i}\kappa h')\delta(h')\mathrm{d}h'=1, \tag{26a}$$

$$\begin{aligned}\gamma_{\mathrm{Vol}}=\exp[\mathrm{i}(\Phi_Q-\kappa h_{\mathrm{g}})]\gamma_{\mathrm{v}},\quad\text{where }\gamma_{\mathrm{v}}&=\frac{1}{D}\int_{h_{\mathrm{v}}-D/2}^{h_{\mathrm{v}}+D/2}\exp(-\mathrm{i}\kappa h')\mathrm{d}h'\\ &=\exp(-\mathrm{i}\kappa h_{\mathrm{v}})\mathrm{sinc}(\kappa D/2).\end{aligned} \tag{26b}$$

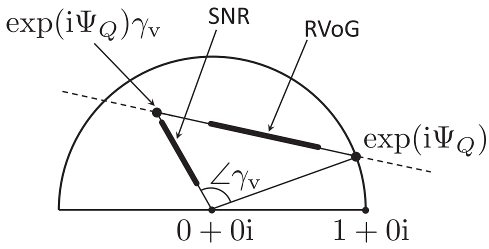

Figure 4. Loci of polarimetric coherence $\gamma(\mathbf{w})$ on the complex plane. The straight line passing through $\exp(\mathrm{i}\Psi_Q)$ and $\exp(\mathrm{i}\Psi_Q)\gamma_{\mathrm{v}}$ is given by formula (27), while the interval marked 'RVoG' corresponds to $0 < m_{\min} \leqslant m(\mathbf{w}) \leqslant m_{\max} < \infty$. The interval marked 'SNR' (which stands for signal to noise ratio) corresponds to formula (67) in appendix C for $0 < \mathrm{SNR}_{\min} \leqslant \mathrm{SNR}(\mathbf{w}) \leqslant \mathrm{SNR}_{\max} < \infty$.

The quantity $\kappa = 2k\Delta\theta/\sin\theta$ is defined in (11). In turn, using (19)–(21) and (26) we obtain:

$$\gamma(\mathbf{w}) = \exp(\mathrm{i}\Psi_Q)\frac{\gamma_{\mathrm{v}} + m(\mathbf{w})}{1 + m(\mathbf{w})} = \exp(\mathrm{i}\Psi_Q)\left(\gamma_{\mathrm{v}} + \frac{m(\mathbf{w})}{1+m(\mathbf{w})}(1-\gamma_{\mathrm{v}})\right) \tag{27}$$

(see appendix B or, e.g., [46]), where

$$\Psi_Q = \Phi_Q - \kappa h_{\mathrm{g}} \quad \text{and} \quad m(\mathbf{w}) = \frac{\sigma_{\mathrm{g}}^2(\mathbf{w})}{\sigma_{\mathrm{v}}^2(\mathbf{w})}. \tag{28}$$

The quantity $m(\mathbf{w})$ in (28), by design, is a non-negative real number. Formula (27) can be visualized by a straight line on the complex plane, see figure 4. Each point on the interval between $\exp(\mathrm{i}\Psi_Q)$ and $\exp(\mathrm{i}\Psi_Q)\gamma_{\mathrm{v}}$ corresponds to a certain value of $m(\mathbf{w})$, $0 \leqslant m(\mathbf{w}) < \infty$.

PolInSAR obtains $\exp(\mathrm{i}\Psi_Q)$ and γ_{v} using relations (27) for different $\mathbf{w}$. Then, the ground topography h_{g}, up to a constant reference elevation, is derived from Ψ_Q using (28), while the average height h_{v} and thickness D of the layer are found from $\angle\gamma_{\mathrm{v}}$ and $|\gamma_{\mathrm{v}}|$, see (26b).

Different physical mechanisms of scattering about the ground and foliage lead to different behavior of σ_{g}^2 and σ_{v}^2 as they depend on the polarization $\mathbf{w}$. Hence, different polarizations $\mathbf{w}$ yield different values of $\gamma(\mathbf{w})$ via equations (27) and (28). On the other hand, the coherence $\gamma(\mathbf{w})$ represents the data for inversion. Indeed, in (25) $\gamma(\mathbf{w})$ is derived from the interferogram $Q(\mathbf{w})$ and intensity $T(\mathbf{w})$, which can be interpreted as observable quantities. Therefore, one can build a straight line fit on the complex plane for the values of $\gamma(\mathbf{w})$ that correspond to several different polarizations $\mathbf{w}$ (see figure 4). Then, according to (27), one of the two intersections of this line with the unit circle $|\gamma| = 1$ shall be associated with $\exp(\mathrm{i}\Psi_Q)$.

However, this procedure alone does not allow one to reconstruct that value of γ_{v} that is needed for obtaining the parameters of the volume scatterer. Indeed, even with $\exp(\mathrm{i}\Psi_Q)$ known, each value of $\mathbf{w}$ used in (27) introduces a new unknown, $m(\mathbf{w})$. Hence, there is still not enough equations to retrieve γ_{v}. For this reason, subsequent steps of inversion that ultimately yield the parameters of the vegetation layer rely on various physical considerations regarding $\sigma_{\mathrm{g}}^2(\mathbf{w})$ and $\sigma_{\mathrm{v}}^2(\mathbf{w})$ [42, 47]. This leads to systems of nonlinear equations with multiple unknowns (e.g., six equations with six unknowns in [21]) that we do not study here. In section 8, we provide specific examples of how one may retrieve the value of γ_{v} in the framework of a simplified RVoG model. PolInSAR with noise is considered in appendix C.

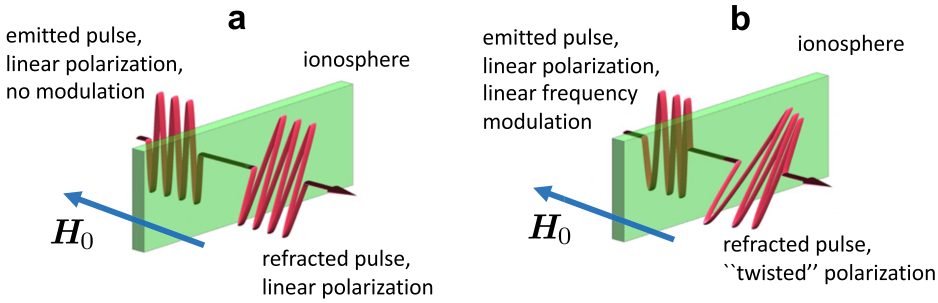

Figure 5. (a) FR for a signal with no frequency modulation. (b) dFR for a linear frequency modulated signal (chirp), see appendix A.

6. Spaceborne polarimetric radar imaging

The electromagnetic field is vector-valued. The polarization specifies the configuration of the electric and magnetic field vectors when radar signals are transmitted and received, as well as when they interact with the target. Hereafter, we rely on the account of polarization given in [23]. A broader scope can be obtained from [8, 42, 48] or the classical sources [49–52].

Radars typically use linearly polarized signals. Each signal, incident or reflected, is a linear combination of the horizontal (H) and vertical (V) polarizations, which gives rise to a 2×2 scattering (or reflectivity) matrix $\mathbf{S}$:

$$\begin{pmatrix} E_{\mathrm{H}}^{\mathrm{sc}} \\ E_{\mathrm{V}}^{\mathrm{sc}} \end{pmatrix}(t,z) = \mathbf{S}(z) \cdot \begin{pmatrix} E_{\mathrm{H}}^{\mathrm{inc}} \\ E_{\mathrm{V}}^{\mathrm{inc}} \end{pmatrix}(t,z), \quad \text{where} \quad \mathbf{S}(z) = \begin{pmatrix} \nu_{\mathrm{HH}}(z) & \nu_{\mathrm{HV}}(z) \\ \nu_{\mathrm{VH}}(z) & \nu_{\mathrm{VV}}(z) \end{pmatrix}. \tag{29}$$

FR is a slow rotation of the polarization plane of a linearly polarized radar pulse in the ionosphere, see figure 5. FR is due to the phenomenon of double circular refraction in a magnetized plasma [52]. Namely, a linearly polarized signal can be represented as a linear combination of two opposite circular polarizations. In a magnetized ionospheric plasma, those two circular polarizations propagate with slightly different speeds. The difference in propagation speeds leads to accumulation of the phase difference between the two circularly polarized signals as they propagate. The phase difference, in turn, results in a rotation of the polarization plane when the original linearly polarized signal is reconstructed from two circular polarizations. The effect of FR on a monochromatic plane wave with frequency ω can be described by means of the rotation matrix (see also figure 5(a)):

$$\mathbf{R}(\varphi_{\mathrm{F}}) = \begin{pmatrix} \cos\varphi_{\mathrm{F}} & \sin\varphi_{\mathrm{F}} \\ -\sin\varphi_{\mathrm{F}} & \cos\varphi_{\mathrm{F}} \end{pmatrix}. \tag{30}$$

The rotation angle in formula (30) is given by (see, e.g., [51–53])

$$\varphi_{\mathrm{F}} \equiv \varphi_{\mathrm{F}}(\omega) = -\frac{R}{2c}\frac{\omega_{\mathrm{pe}}^2\Omega_{\mathrm{e}}\cos\beta}{\omega^2}, \quad \text{where}\, \omega_{\mathrm{pe}}^2 = \frac{4\pi N_{\mathrm{e}}e^2}{m_{\mathrm{e}}}, \quad \Omega_{\mathrm{e}} = -\frac{e|\boldsymbol{H}_0|}{m_{\mathrm{e}}c}. \tag{31}$$

In (31), ω_{pe} and Ω_{e} are the electron plasma frequency and gyrofrequency, respectively, m_{e} and $-e$ are the mass and charge of the electron, N_{e} denotes the electron number density in the ionosphere, $\boldsymbol{H}_0$ is the magnetic field of the Earth, β is the angle between the wave propagation direction and $\boldsymbol{H}_0$, and R is the propagation distance.

The FR angle φ_{F} in (30) depends on the frequency ω via (31). The instantaneous frequency $\omega = \omega(t)$ of the chirp varies between $\omega_0 - B/2$ and $\omega_0 + B/2$, see appendix A. Hence, the FR angle also varies across the chirp bandwidth, a phenomenon known as dFR. Due to dFR, a linearly polarized chirp becomes 'twisted' after passing through a magnetized plasma, see [23] and figure 5(b).

The propagation of radar signals in the ionosphere is affected by the dispersion of electric permittivity in the plasma, and one needs to take it into account when building the image (see [37, 38] or [39, chapter 3]). The resulting polarimetric channels are convenient to arrange as entries of a 2×2 matrix $\mathbf{Y}$ that is called the intermediate image (cf equation (29)):

$$Y_{mn}(\boldsymbol{y}) = \int \exp[\mathrm{i}\omega_0(t - 2R_{\boldsymbol{y}}/v_{\mathrm{ph}})]\overline{A_2'(t,\boldsymbol{y})}u_{mn}^{\mathrm{sc}}(t)\mathrm{d}t, \quad m,n \in \{\mathrm{H},\mathrm{V}\}, \tag{32}$$

where the scattered field $u_{mn}^{\mathrm{sc}}(t) = E_m^{\mathrm{sc}}(t,\boldsymbol{x})$ corresponds to the emitted polarization n and the chirp envelope $A_2'(t,\boldsymbol{y}) = \chi_{\tau-2\delta\tau}'(t - 2R_{\boldsymbol{y}}/v_{\mathrm{gr}})\exp[-\mathrm{i}(\alpha + 2\delta\alpha)(t - 2R_{\boldsymbol{y}}/v_{\mathrm{gr}})^2]$ accounts for the round-trip propagation. This envelope, the phase and group velocity v_{ph} and v_{gr}, and variations of chirp parameters $\delta\tau$ and $\delta\alpha$ due to the ionosphere are introduced in appendix A.

Next, the mean rotation angle is defined using (31): $\varphi_{\mathrm{F}}^* = \varphi_{\mathrm{F}}(\omega_0)$, and the rotation matrices $\mathbf{R}(-\varphi_{\mathrm{F}}^*)$ are applied to $\mathbf{Y}$ of (32), which yields a 2×2 polarimetric image matrix $\mathbf{I}$:[5]

$$\mathbf{I}(\boldsymbol{y}) = \mathbf{R}(-\varphi_{\mathrm{F}}^*) \cdot \mathbf{Y}(\boldsymbol{y}) \cdot \mathbf{R}(-\varphi_{\mathrm{F}}^*). \tag{33}$$

The mean rotation angle in (33) creates a mismatch between the actual FR angle and φ_{F}^*:

$$\Delta\varphi_{\mathrm{F}} \equiv \Delta\varphi_{\mathrm{F}}(t,\boldsymbol{z}) = \varphi_{\mathrm{F}}\left(\omega(t - 2R_{\boldsymbol{z}}/c)\right) - \varphi_{\mathrm{F}}^*. \tag{34}$$

In [23], we have introduced and analyzed a mitigation technique for the mismatch, called the PMF. We will not be considering the PMF hereafter, as our goal is rather to assess the effect of dFR on PolInSAR when standard processing is used.

The polarimetric imaging operator is given by (cf formula (1))

$$\boldsymbol{I}(\boldsymbol{y}) = \int \mathbf{W}(\boldsymbol{y},\boldsymbol{z}) \cdot \nu(\boldsymbol{z})\mathrm{d}\boldsymbol{z}, \tag{35}$$

where (cf equation (29))

$$\boldsymbol{I} = (I_{\mathrm{HH}}, I_{\mathrm{HV}}, I_{\mathrm{VH}}, I_{\mathrm{VV}})^{\mathrm{T}}, \qquad \nu = (\nu_{\mathrm{HH}}, \nu_{\mathrm{HV}}, \nu_{\mathrm{VH}}, \nu_{\mathrm{VV}})^{\mathrm{T}},$$

and the 4×4 matrix $\mathbf{W}$ is defined as follows:

$$\mathbf{W}(\boldsymbol{y},\boldsymbol{z}) = \exp[-2\mathrm{i}k(R_{\boldsymbol{y}} - R_{\boldsymbol{z}})] \int \overline{A\left(t - \frac{2R_{\boldsymbol{y}}}{c}\right)} A\left(t - \frac{2R_{\boldsymbol{z}}}{c}\right) \mathbf{V}(\Delta\varphi_{\mathrm{F}})\mathrm{d}t. \tag{36}$$

In (36), $\Delta\varphi_{\mathrm{F}}(t,\boldsymbol{z})$ is given by (34) and the matrix $\mathbf{V}$ is

$$\mathbf{V}(\phi) = \begin{pmatrix} \cos^2\phi & -\cos\phi\sin\phi & \cos\phi\sin\phi & -\sin^2\phi \\ \cos\phi\sin\phi & \cos^2\phi & \sin^2\phi & \cos\phi\sin\phi \\ -\cos\phi\sin\phi & \sin^2\phi & \cos^2\phi & -\cos\phi\sin\phi \\ -\sin^2\phi & -\cos\phi\sin\phi & \cos\phi\sin\phi & \cos^2\phi \end{pmatrix}. \tag{37}$$

[5] During the signal round-trip between the spaceborne antenna and the target, the FR angle doubles rather than cancels (see [23, 54] or [39, chapter 5]).

Equation (36) is derived in [23, section 3.3]. It incorporates the original pulse envelope A rather than the modified envelope A (see appendix A) because, according to [39, section 3.11], if one properly takes the ionospheric dispersion into account, the resulting image is basically the same as it would have been in the truly dispersionless case. Therefore, the effect of dFR on spaceborne polarimetric imaging is fully accounted for via the matrix $\mathbf{V}(\Delta\varphi_{\mathrm{F}})$ in (36).

7. The effect of dFR on polarimetric imaging

Linearization of $\varphi_{\mathrm{F}}(\omega)$ about ω_0 in (34) yields:

$$\Delta\varphi_{\mathrm{F}} \approx \eta \frac{1}{\tau}\left(t - \frac{2R_z}{c}\right), \quad \text{where } \eta = -\varphi_{\mathrm{F}}(\omega_0)\frac{2B}{\omega_0}. \tag{38}$$

Substituting (38) into the integrand of (36), we obtain the imaging kernel matrix:

$$\mathbf{W} = \exp[-2\mathrm{i}k(R_y - R_z)] \begin{pmatrix} V_0 & -V_1 & V_1 & -V_2 \\ V_1 & V_0 & V_2 & V_1 \\ -V_1 & V_2 & V_0 & -V_1 \\ -V_2 & -V_1 & V_1 & V_0 \end{pmatrix}. \tag{39}$$

The entries of the matrix $\mathbf{W}$ are functions of two variables: $\xi = B(R_y - R_z)/c$ and η:

$$V_0(\xi;\eta) = \frac{\tau}{2}\left(\operatorname{sinc}\xi + F_0(\xi;\eta)\right), \quad V_1(\xi;\eta) = \frac{\tau}{2\mathrm{i}}F_1(\xi;\eta), \quad V_2(\xi;\eta) = \frac{\tau}{2}\left(\operatorname{sinc}\xi - F_0(\xi;\eta)\right), \tag{40}$$

where

$$F_0(\xi;\eta) = \frac{1}{2}\left(\operatorname{sinc}(\xi-\eta) + \operatorname{sinc}(\xi+\eta)\right) \quad \text{and}$$
$$F_1(\xi;\eta) = \frac{1}{2}\left(\operatorname{sinc}(\xi-\eta) - \operatorname{sinc}(\xi+\eta)\right). \tag{41}$$

One can see that as $\eta \to 0$ (or as $\varphi_{\mathrm{F}} \to 0$, see (38)), the matrices in (37) and (39) become diagonal, and the matrix imaging operator in (35) transforms into a set of scalar imaging operators acting on individual reflectivity channels, see (1).

The L_2 norms of the matrix entries in (39) were computed in [23]. For small η, we have:

$$\frac{\|V_1\|_2^2(\eta)}{\|V_0\|_2^2(\eta)} \approx \frac{\eta^2}{12}, \qquad \frac{\|V_2\|_2^2(\eta)}{\|V_0\|_2^2(\eta)} \approx \frac{\eta^4}{80}. \tag{42}$$

The asymptotic expressions (42) work well up to $|\eta| \lesssim 1$. We see that for $|\eta| \lesssim 1$, the leading off-diagonal terms of $\mathbf{W}$ are due to V_1. In addition, for $|\eta| \ll 1$ one can derive:

$$F_0(\xi;\eta) \approx \frac{1}{\tau}V_0(\xi;\eta) \approx \operatorname{sinc}\xi \quad \text{and} \quad F_1(\xi;\eta) = \frac{2\mathrm{i}}{\tau}V_1(\xi;\tau) \approx -\eta\operatorname{sinc}'\xi. \tag{43}$$

The behavior of $F_0(\xi;\ \eta)$ and $F_1(\xi;\ \eta)$ of (43) is schematically shown in figure 3.

Table 1. Notation for the simplified RVoG model (44).

Traditional notation	New notation	Ground reflectivity	Volume reflectivity
HH	C	$\sigma^2_{\mathrm{C,g}}$	$\sigma^2_{\mathrm{C,v}}$
HV or VH	X	0	$\sigma^2_{\mathrm{X,v}}$
VV	Not represented	—	—

8. Polarimetric interferometry in the presence of dFR

8.1. A simplified RVoG model

To understand the effect of dFR on PolInSAR, we first build a simplified model that would still support the key properties of polarimetric geophysical observations. Our analysis will focus on one of the most popular PolInSAR tasks, namely, the reconstruction of parameters of the aboveground vegetation layer.

In the RVoG model, see (19)–(21), one specifies the reflectivities of the ground, $\sigma^2_{\mathrm{g}}(\mathbf{w})$, and volume, $\sigma^2_{\mathrm{v}}(\mathbf{w})$, for at least two different values of $\mathbf{w}$. Hereafter, we will associate different values of $\mathbf{w}$ with different polarimetric scattering channels. Moreover, we introduce a simplified polarimetric setting in this section that involves only two different channels: one co-polarized channel (denoted by $\mathbf{w} = \mathrm{C}$) and one cross-polarized channel (denoted by $\mathbf{w} = \mathrm{X}$). Using the traditional notation of section 6, these channels can be interpreted as shown in table 1.

Accordingly, the reflectivity of the scatterer in these two channels is given by

$$\sigma^2_{\mathrm{C}}(h) = \sigma^2_{\mathrm{C,g}}\delta(h - h_{\mathrm{g}}) + \sigma^2_{\mathrm{C,v}}\frac{1}{D}\chi_D(h - h_{\mathrm{g}} - h_{\mathrm{v}}), \tag{44a}$$

$$\sigma^2_{\mathrm{X}}(h) = \sigma^2_{\mathrm{X,v}}\frac{1}{D}\chi_D(h - h_{\mathrm{g}} - h_{\mathrm{v}}). \tag{44b}$$

The physical rationale behind the model (44) is as follows. Scattering from the ground contributes only to the co-polarized channel, C, see (44a), because the asymptotic models supported by observations indicate that the ground contribution to the cross-polarized scattering is very small [42, 55, 56], hence, $\sigma^2_{\mathrm{X,g}} = 0$. At the same time, ground reflectivity may dominate the radar return on HH-polarization, which could be explained by the ground-trunk double-bounce mechanism [19, 57]. Therefore, we exclude the VV channel from subsequent consideration. For the foliage, the microscopic reflectivity models [42] yield comparable values for the co-polarized and cross-polarized channels, so we employ two separate constants, $\sigma^2_{\mathrm{C,v}}$ an $\sigma^2_{\mathrm{X,v}}$, to describe the volume reflectivity in these two channels.

Altogether, equation (44) represent a further simplification of the model (21).

Recall that the cross-talk between the interferometric channels due to dFR is described by the off-diagonal entries of the imaging kernel (39). This effect is controlled by the value of the parameter $\eta = -\varphi_{\mathrm{F}}(\omega_0) \cdot 2B/\omega_0$, see (38). In the interferometric setting, due to the sub-band selection as in (9), we introduce

$$\tilde{\eta} = \eta \cdot \frac{\tilde{B}}{B}. \tag{45}$$

Sub-banding also shifts the central frequencies of the two frequency bands:

$$\varphi^{*(1)}_{\mathrm{F}} = \varphi_{\mathrm{F}}(\omega_1), \qquad \varphi^{*(2)}_{\mathrm{F}} = \varphi_{\mathrm{F}}(\omega_2), \tag{46}$$

where ω_1 and ω_2 are defined in (9). The mean rotation angles (46) will be used for building the corresponding intermediary images in (33) instead of $\varphi_F^* = \varphi_F(\omega_0)$. Note also that the last column and last row of the matrix (39) will not be used because the VV channel is not included in the simplified RVoG model presented in table 1.

Interferometric coherences in the case of cross-talk due to dFR can be obtained similarly to (26). Assuming $|\eta| < 1$ (thus, $|\tilde{\eta}| < 1$), see [23], we can use (42) and drop the terms $\propto V_2$ in the matrix (39). We additionally assume that the reflectivities in the channels C and X do not correlate[6]. Then, using the reflectivity model (44), imaging model (35), and definitions (8) and (23), we obtain the complex interferograms Q_C, Q_X and intensities T_C, T_X:

$$\begin{aligned} Q_C &= \exp(i\Psi_Q)\left(V_{Q0}(\sigma^2_{C,g} + \sigma^2_{C,v}\gamma_v) + 2V_{Q1}\sigma^2_{X,v}\gamma_v\right), \\ Q_X &= \exp(i\Psi_Q)\left(V_{Q0}\sigma^2_{X,v}\gamma_v + V_{Q1}(\sigma^2_{C,g} + \sigma^2_{C,v}\gamma_v)\right), \\ T_C &= V_{Q0}(\sigma^2_{C,g} + \sigma^2_{C,v}) + 2V_{Q1}\sigma^2_{X,v} + \mathbf{N}^2, \\ T_X &= V_{Q0}\sigma^2_{X,v} + V_{Q1}(\sigma^2_{C,g} + \sigma^2_{C,v}) + \mathbf{N}^2. \end{aligned} \tag{47}$$

In formulae (47), Ψ_Q is defined in (28), $\mathbf{N}^2$ is the intensity of noise defined in appendix C, and (cf equation (18))

$$\begin{aligned} V_{Q0} \equiv V_{Q0}(\eta) &= \int |V_0(\tilde{B}s \sin\theta/c; \tilde{\eta})|^2 \, ds, \\ V_{Q1} \equiv V_{Q1}(\eta) &= \int |V_1(\tilde{B}s \sin\theta/c; \tilde{\eta})|^2 ds, \end{aligned} \tag{48}$$

where $V_0(\xi;\ \eta)$ and $V_1(\xi;\ \eta)$ are given in (40)–(43). As in section 5, we assume in (47) that the intensities of the two images are the same and use T_C and T_X instead of $\sqrt{T_C^{(1)}T_C^{(2)}}$ and $\sqrt{T_X^{(1)}T_X^{(2)}}$. The coefficient 2 in the expressions for Q_C and T_C in (47) reflects the fact that the notation X represents two actual polarimetric channels, see table 1, each affecting the C channel via cross-talk due to dFR.

From (47), we can obtain the interferometric coherences in the specified channels similarly to (25), and, additionally, the cross-channel intensity ratio:

$$\gamma_C = \frac{Q_C}{T_C}, \qquad \gamma_X = \frac{Q_X}{T_X}, \qquad M = \frac{T_C}{T_X}. \tag{49}$$

In (47), $\exp(i\Psi_Q)$ is unknown as discussed after equations (27) and (28). The determination of $\exp(i\Psi_Q)$ is equivalent to the reconstruction of the local elevation. Another parameter to be retrieved is γ_v that carries the information about the mean elevation h_v and thickness D of the scattering volume above ground (the vegetation layer), see (26b). We will consider the left-hand sides in (49) as the data for inversion. Note that $\sigma^2_{C,g}$, $\sigma^2_{C,v}$, $\sigma^2_{X,v}$, and $\mathbf{N}^2$ are also considered unknown, so there are not enough equations to determine all the unknowns. Nonetheless, the ground topography and geometry of the vegetation layer can be reconstructed in certain special cases, as we discuss below.

A simple example of PolInSAR reconstruction can be obtained from a bare-bone model

$$V_{Q1} = 0, \qquad \mathbf{N}^2 = 0, \quad \text{and} \quad \sigma^2_{C,v} = 0. \tag{50}$$

[6] Note that the observations [6, 56] show high correlation between the co-polarized channels in the reflection from the ground. It does not affect the model (44) since it contains only one co-polarized channel.

Assumptions (50) make the polarimetric channels decoupled and affected only by one component of the scatterer, namely, ground and foliage affect the C and X channels, respectively. As a result, the first two expressions in (49) yield:

$$\gamma_{\mathrm{C}} = \exp(\mathrm{i}\Psi_Q), \qquad \gamma_{\mathrm{X}} = \exp(\mathrm{i}\Psi_Q)\gamma_{\mathrm{v}}. \tag{51}$$

Relations (51) can be considered as the extreme cases of (27) for $m(\mathbf{w}) = \infty$ and $m(\mathbf{w}) = 0$, respectively. The reconstruction of the vegetation layer parameters from the data γ_{C} and γ_{X} in this case can be performed easily with the help of (26):

$$\Psi_Q = \angle\gamma_{\mathrm{C}}, \tag{52a}$$

$$h_{\mathrm{v}} = -\frac{1}{\kappa}\angle\gamma_{\mathrm{v}} = -\frac{1}{\kappa}\angle\frac{\gamma_{\mathrm{X}}}{\gamma_{\mathrm{C}}}, \tag{52b}$$

$$D = \frac{2}{\kappa}\,\mathrm{sinc}^{-1}\,|\gamma_{\mathrm{v}}| = \frac{2}{\kappa}\,\mathrm{sinc}^{-1}\left|\frac{\gamma_{\mathrm{X}}}{\gamma_{\mathrm{C}}}\right|, \tag{52c}$$

where $\mathrm{sinc}^{-1}(\zeta)$ is the inverse function to $\zeta = \mathrm{sinc}\,\xi$ for $0 \leqslant \zeta \leqslant 1$. We see that h_{v} will not exceed the height ambiguity threshold specified in (15), and $D \leqslant h_{\mathrm{v}}/2$ by design, see figure 3.

Of course, the reconstruction (52) cannot reveal any effect due to dFR because the latter requires a nonzero value of the parameter V_{Q1} in (47), whereas in (50) we have $V_{Q1} = 0$. To understand the role of dFR, we consider two more realistic scenarios where the polarimetric channels do not decouple ($\sigma^2_{\mathrm{C,v}} \neq 0$): noiseless (see section 8.2) and with noise (see section 8.3). In each of these scenarios, one can obtain a quantitative assessment of the effect of dFR on PolInSAR reconstruction, and in section 8.4 we perform the corresponding analysis for the more comprehensive case that involves noise.

8.2. Noiseless PolInSAR

In this scenario, we make two simplifications regarding system (47) and (49). First, we introduce the ratios between the reflectivity values in table 1 as follows:

$$\mathcal{A} = \frac{\sigma^2_{\mathrm{C,v}}}{\sigma^2_{\mathrm{X,v}}}, \qquad \mu = \frac{\sigma^2_{\mathrm{C,g}}}{\sigma^2_{\mathrm{X,v}}}, \tag{53}$$

and assume that the quantity $\mathcal{A}$ is known, i.e., we do not need to reconstruct it using PolInSAR. The rationale is that $\mathcal{A}$ in (53) can be measured experimentally in a variety of practical conditions. Second, we remove the noise term by setting $\mathbf{N}^2 = 0$. In addition, we introduce the quantity q to characterize the magnitude of the dFR effect:

$$q = \frac{V_{Q1}}{V_{Q0}} \approx \frac{1}{12}\tilde{\eta}^2, \tag{54}$$

see (42), (45), and (48). As a result, we obtain the following expressions for the coherences and cross-channel intensity defined in (49):

$$\begin{aligned} \gamma_{\mathrm{C}} &= \exp(\mathrm{i}\Psi_Q)\left(1 + \frac{\mathcal{A}+2q}{\mu+\mathcal{A}+2q}(\gamma_{\mathrm{v}}-1)\right), \\ \gamma_{\mathrm{X}} &= \exp(\mathrm{i}\Psi_Q)\left(\gamma_{\mathrm{v}} + \frac{q\mu}{1+q(\mu+\mathcal{A})}(1-\gamma_{\mathrm{v}})\right), \\ M &= \frac{\mu+\mathcal{A}+2q}{1+q(\mu+\mathcal{A})}. \end{aligned} \tag{55}$$

The first two equations in (55) resemble (27). Each of the two yields a complex value on the segment of a straight line between $\exp(\mathrm{i}\Psi_Q)$ and $\exp(\mathrm{i}\Psi_Q)\gamma_\mathrm{v}$ (see figure 4). Compared to (51), the points γ_C and γ_X would shift towards each other starting from the points $\exp(\mathrm{i}\Psi_Q)$ and $\exp(\mathrm{i}\Psi_Q)\gamma_\mathrm{v}$, respectively.

Setting $q = 0$ in equation (55) corresponds to dropping dFR from consideration:

$$\begin{aligned} \gamma_\mathrm{C} &= \exp(\mathrm{i}\Psi_Q)\left(1 + \frac{\mathcal{A}}{\mu + \mathcal{A}}(\gamma_\mathrm{v} - 1)\right), \\ \gamma_\mathrm{X} &= \exp(\mathrm{i}\Psi_Q)\gamma_\mathrm{v}, \\ M &= \mu + \mathcal{A}. \end{aligned} \tag{56}$$

As long as $\mathcal{A} \neq 0$, system (56) is not equivalent to the simplified model based on (50). Given the left-hand sides $\gamma_\mathrm{C} \in \mathbb{C}$, $\gamma_\mathrm{X} \in \mathbb{C}$, and $M \in \mathbb{R}$ as the data, equation (56) can be solved for $\gamma_\mathrm{v} \in \mathbb{C}$, $\Psi_Q \in \mathbb{R}$, $\mu \in \mathbb{R}$, and $\mathcal{A} \in \mathbb{R}$. This is trivial if the data are obtained using the same reduced model (56). However, if on the left-hand side of (56) we substitute the data that account for dFR, i.e., the data generated by (55) with $q \neq 0$, then the quantities γ_v', Ψ_Q', μ', and $\mathcal{A}'$ found by solving (56) will, generally speaking, differ from those used in (55) when generating the data γ_C, γ_X, and M.[7] The resulting discrepancy can be used to quantify the effect of dFR on the noiseless PolInSAR inversion. We, however, do not derive these estimates and rather proceed directly to a more comprehensive case that includes noise.

8.3. PolInSAR with noise

Similarly to section 8.2, we assume that the quantity $\mathcal{A}$ defined in (53) is known. To introduce PolInSAR with noise, we consider $\mathbf{N}^2 > 0$ and in the meantime, take $q = 0$. Instead of using a polarization-dependent SNR as in appendix C, we will parameterize the noise term in (47) with the help of

$$n_\mathrm{g} = \frac{\mathbf{N}^2}{V_{Q0}\sigma^2_{\mathrm{C,g}}} = \text{const.} \tag{57}$$

Then, for the quantities defined in (49) we have:

$$\gamma_\mathrm{C} = \exp(\mathrm{i}\Psi_Q)\frac{\mu + \gamma_\mathrm{v}\mathcal{A}}{\mu + \mathcal{A} + n_\mathrm{g}\mu}, \tag{58a}$$

$$\gamma_\mathrm{X} = \exp(\mathrm{i}\Psi_Q)\frac{\gamma_\mathrm{v}}{1 + n_\mathrm{g}\mu}, \tag{58b}$$

$$M = \frac{\mu + \mathcal{A} + n_\mathrm{g}\mu}{1 + n_\mathrm{g}\mu}. \tag{58c}$$

Equation (58b) is equivalent to (67), except that it uses different notation, see (44), (53), and (57). This is not surprising because in the absence of dFR, the imaging operator $\mathbf{W}$ of (35) is diagonal, so the X channel is due entirely to the volume scatterer, see (44).

The inversion is done as follows. With the left-hand sides of (58) considered as data, we solve this system for the unknown γ_v, Ψ_Q, μ, and n_g. As γ_v is complex-valued, this yields a

[7] Solution of system (56) includes the value of $\mathcal{A}$ that, as indicated previously, can be obtained by experimental measurements and does not need to be reconstructed by dFR. If (56) is solved with the data that have dFR, the mismatch between the resulting $\mathcal{A}'$ and true $\mathcal{A}$ also shows the effect of dFR on PolInSAR.

total of 5 real-valued unknowns. Equations (58a) and (58b) are also complex-valued, making the number of equations equal to the number of unknowns. The key step in finding a closed form solution is to eliminate γ_v from equations (58a) and (58b) and extract $\exp(\mathrm{i}\Psi_Q)$:

$$\exp(\mathrm{i}\Psi_Q) = \left(1 + \frac{\mathcal{A}}{\mu} + n_g\right)\left(\gamma_C - \gamma_X \frac{\mathcal{A}}{M}\right). \tag{59}$$

We obtain Ψ_Q as $\Psi_Q = \angle\left(\gamma_C - \gamma_X \mathcal{A} M^{-1}\right)$ because $1 + \mathcal{A}\mu^{-1} + n_g \in \mathbb{R}$. After that, the first equation of (28) yields the ground topography h_g. Taking the absolute value on both sides of (59) yields:

$$1 + \frac{\mathcal{A}}{\mu} + n_g = |\Gamma|^{-1}, \quad \text{where} \quad \Gamma = \gamma_C - \gamma_X \frac{\mathcal{A}}{M}. \tag{60}$$

Equations (60) and (58c) are solved as a system for μ and n_g; from the physical considerations, both values should be non-negative. Finally, from (58b) we derive:

$$\gamma_v = \gamma_X \frac{|\Gamma|}{\Gamma}(1 + n_g \mu) \tag{61}$$

and using (26b), obtain (cf formulae (52b) and (52c)):

$$h_v = -\frac{1}{\kappa}\angle\gamma_v \quad \text{and} \quad D = \frac{2}{\kappa}\,\mathrm{sinc}^{-1}\,|\gamma_v|. \tag{62}$$

The resulting quantities h_g, h_v, and D are the geophysical characteristics of interest of the vegetation-covered terrain, see figure 3. We should emphasize that this inversion is exact as long as there is no dFR ($q = 0$) and the observables γ_C, γ_X, and M obey (58).

8.4. The effect of dFR on PolInSAR inversion

To quantify the effect of dFR on PolInSAR with noise, system (58) should be solved with the data γ_C, γ_X, and M that account for dFR. To generate such data, we specify some physically meaningful values of $q > 0$, γ_v, Ψ_Q, $\mathcal{A}$, and μ. As far as the noise, one particular choice may be $n_g = 0$, in which case the subject-to-dFR data are obtained according to (55).[8] Otherwise, we may have $n_g > 0$ as well, as in the following system that is obtained from (47) and (49) without simplifications:

$$\begin{aligned}
\gamma_C &= \exp(\mathrm{i}\Psi_Q)\frac{\mu + \gamma_v(\mathcal{A} + 2q)}{\mu + \mathcal{A} + 2q + n_g\mu},\\
\gamma_X &= \exp(\mathrm{i}\Psi_Q)\frac{\gamma_v + q(\mu + \mathcal{A}\gamma_v)}{1 + q(\mu + \mathcal{A}) + n_g\mu},\\
M &= \frac{\mu + \mathcal{A} + 2q + n_g\mu}{1 + q(\mu + \mathcal{A}) + n_g\mu}.
\end{aligned} \tag{63}$$

The system (63) reduces to (55) and (58) for $n_g = 0$ and $q = 0$, respectively.

We invert the data that account for dFR as in section 8.3, see formulae (59)–(62). We will use primes to denote the output of this inversion, e.g., Ψ'_Q and γ'_v. In doing so, we may expect some discrepancies: $\Psi'_Q \neq \Psi_Q$ and/or $\gamma'_v \neq \gamma_v$, because the reconstruction in section 8.3 assumes

[8] The first equation of (55) implies, in particular, that $|\gamma_C| < 1$, which means that the co-polarized channel is decorrelated.

$q = 0$. The effect of dFR on PolInSAR will be characterized precisely by the magnitude of those discrepancies. For the actual examples that we present, they are computed numerically. In section 9, we briefly describe an even more comprehensive scenario that may be considered an alternative to what we do here for the purpose of assessing the effect of dFR on PolInSAR.

In turns out that the reconstructed geophysical parameters given by (60)–(62) are not affected by the presence of noise in the full system (63) as compared to (55). In particular, for the data calculated according to (63), we have (cf formulae (59) and (60)):

$$\Gamma' = \exp(\mathrm{i}\Psi_Q)\frac{\mu + q(2\gamma_\mathrm{v} - \mathcal{A}\mu - \mathcal{A}^2\gamma_\mathrm{v})}{\mu + \mathcal{A} + 2q + n_\mathrm{g}\mu}.$$

The only appearance of n_g in the previous expression is in the denominator, and since the latter is a real number, the value of $\exp(\mathrm{i}\Psi'_Q) = \Gamma'/|\Gamma'|$ does not depend on n_g. Similarly, it can be shown that formula (61) yields

$$\gamma'_\mathrm{v} = \exp[\mathrm{i}(\Psi_Q - \Psi'_Q)] \\ \times \frac{(1-\mathcal{A})\,(\gamma_\mathrm{v} + q(\mu + \mathcal{A}\gamma_\mathrm{v}))}{1 + q(\mu + \mathcal{A}) - (\mu + \mathcal{A} + 2q) + |\mu + q(2\gamma_\mathrm{v} - \mathcal{A}\mu - \mathcal{A}^2\gamma_\mathrm{v})|},$$

and this expression does not depend on n_g either. Hence, in our results below, the data are obtained by the noise-free formulae (55).

The effect of dFR manifests itself via systematic reconstruction discrepancies, or errors, in the ground topography and vegetation layer properties, i.e., its average elevation and thickness. The magnitude of the effect depends on several groups of parameters. One group includes the radar system parameters, such as its carrier frequency and bandwidth, see appendix A. Another group consists of the ionospheric parameters that define the FR, such as the local magnetic field and electron concentration, see (31). Yet the third group of parameters are related to radar interferometry. It includes the interferometric wavenumber κ (which, in turn, is defined by the interferometric angle $\Delta\theta$, see (11)) and the parameters of the scatterer: Ψ_Q, γ_v, μ, $\mathcal{A}$, etc, see sections 5 and 8.1. Eventually, these parameters are combined into the coefficients and unknowns of systems (55) and (58).

For our simulations, we take the ionospheric and imaging parameters as in [23], namely, the TEC of 50 TECU, $|\boldsymbol{H}^{(0)}| = 0.5$ Gs, and parallel propagation. For interferometry, we set $\tilde{B}/B = 0.85$. Substituting this into (9) and (15), we obtain $\Delta\theta \approx 0.007$ rad and the ambiguity height of about 60 m, respectively.

Figure 6 displays the reconstruction errors as functions of γ_v (see (26b)). Figure 6(a) illustrates the errors in Ψ_Q, which characterize the effect of dFR on the derived ground topography, see (28). Figure 6(b) presents the reconstruction error for the complex coherence of the volume scatterer, while the effect on the elevation and thickness of the foliage layer is illustrated by figures 6(c) and (d), respectively. However, the last two of these metrics have anomalies in the vicinity of the origin, whereas the underlying error in the complex coherence (panel (b)) has no such irregularities. From the inversion formulae (61) and (62) we determine that the errors can be particularly high when the value of $|\gamma_\mathrm{X}|$ in (55) is small, because small $|\gamma_\mathrm{X}|$ implies small $|\gamma_\mathrm{v}|$. We exclude this anomalous behavior by setting a threshold $\zeta = 1/2$ on the value of $|\gamma_\mathrm{v}|$ when calculating an error metric. In particular, if $f(\alpha, \gamma_\mathrm{v})$ is any of the error metrics

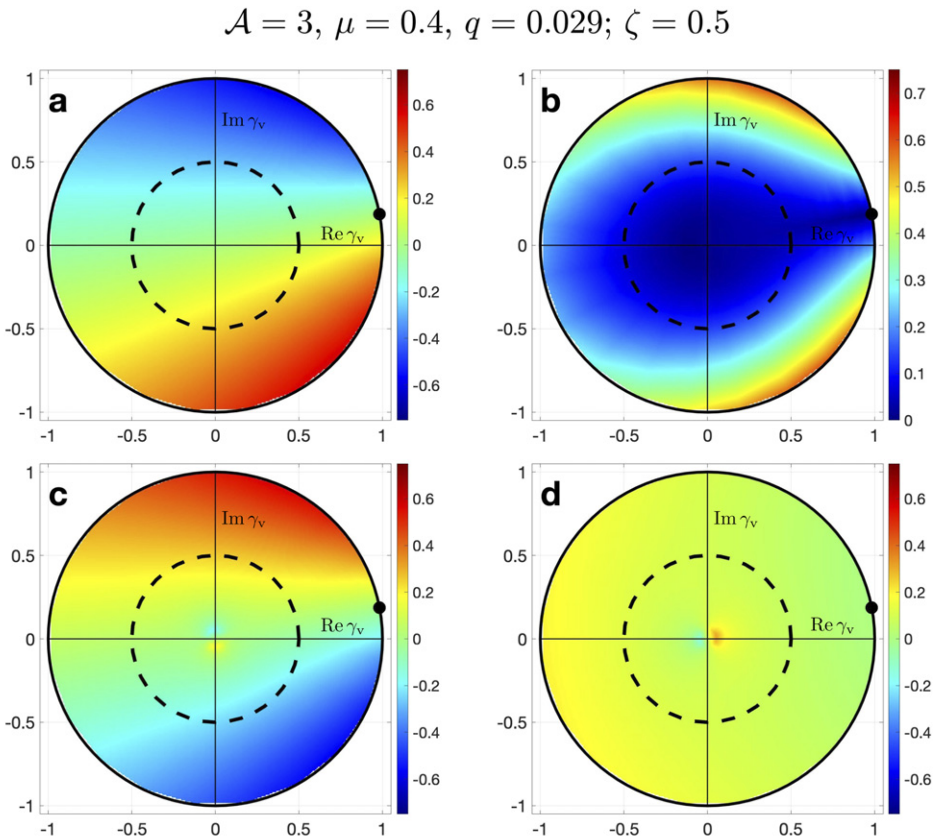

Figure 6. Reconstruction errors according to section 8.4, as functions of (Re γ_v, Im γ_v). The true value of $\exp(i\Psi_Q)$ is shown by a black dot. (a) $\Psi'_Q - \Psi_Q$; (b) $|\gamma'_v - \gamma_v|$; (c) $\angle(\gamma'_v/\angle\gamma_v)$; (d) $|\gamma'_v/\gamma_v| - 1$. The dashed circle corresponds to the threshold value ζ in (64). The effect of these errors on the topography and parameters of the vegetation layer (see figure 3) can be calculated using (62) and the first equation of (28).

shown in figure 6 and α denotes any parameter other than γ_v, then we use the threshold ζ in the following definition of the error function f_α:

$$f_\alpha(\alpha;\zeta) = \max_{\zeta \leqslant |\gamma_v| \leqslant 1} |f(\alpha, \gamma_v)|. \tag{64}$$

The value of $\zeta = 1/2$ corresponds to the radius of the dashed circles in figure 6.

In figure 7, we show how the reconstruction errors depend on the parameter q of (54) that controls the magnitude of the dFR effect for two different values of the parameter $\mathcal{A}$. These errors are defined according to (64) and characterize the reconstruction of Ψ_Q, h_v, and D. Additionally, in figure 7 we show the values of q for three spaceborne radar systems considered in the literature [23, 25, 58], with the ionospheric parameters as in [23]. An arbitrarily chosen error threshold of 0.3 (or 30%) is also shown on the plots. Errors above this level can be considered significant for most applications. Additional error plots for the values of q that correspond to the BIOMASS satellite are given in figure 8. We see that in most cases, the error level is below the chosen threshold. For other existing SAR satellites that operate on higher frequencies (C-band or X-band) the effect of dFR will be even weaker (the corresponding vertical lines in figure 7

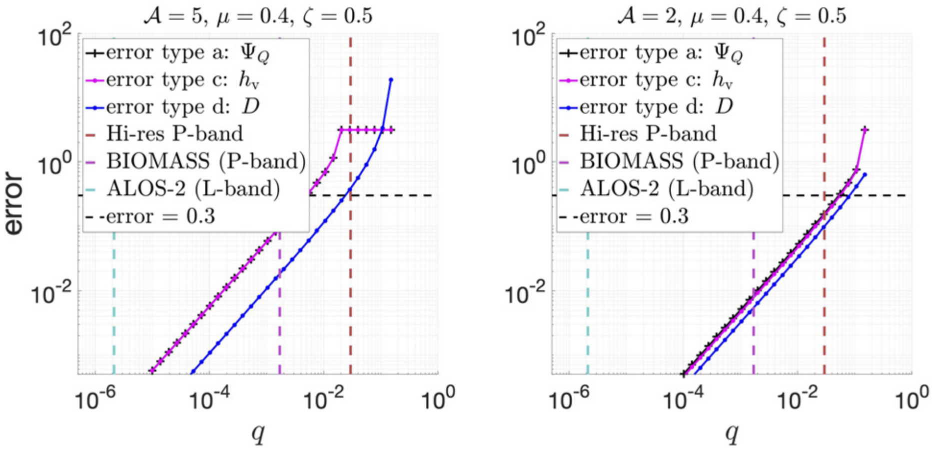

Figure 7. Reconstruction errors as per section 8.4 vs q of (54) for two different values of the parameter $\mathcal{A}$, see (44). The three colored curves represent the error (64) for the quantities displayed in panels (a), (c) and (d) of figure 6, which correspond to the reconstruction of Ψ_Q, h_{v}, and D, respectively, see (62) and the first equation of (28). The dashed vertical line 'Hi-res P-band' corresponds to the system described in [23]. The BIOMASS and ALOS-2 systems are described in [25, 58], respectively. The upper limit on the value of q is set by the condition that the reconstructed values of μ and n_{g} are non-negative, see section 8.3.

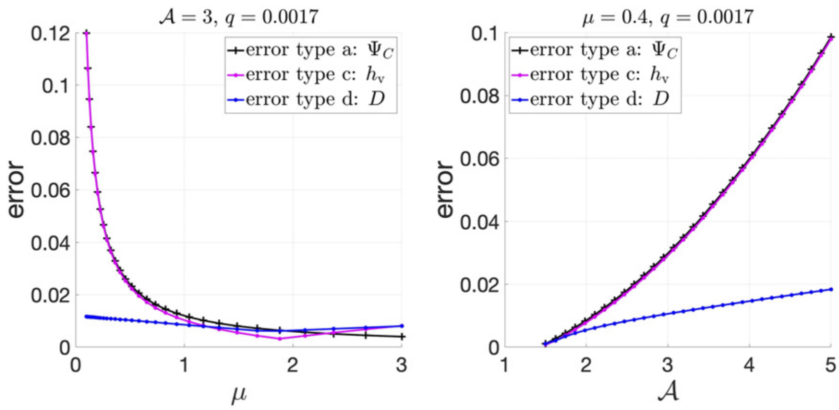

Figure 8. Dependence of the reconstruction errors as per section 8.4 on μ (left) and $\mathcal{A}$ (right). The value of $q = 0.0017$ corresponds to the BIOMASS system.

would be further to the left) because the FR angle is inversely proportional to the square of the frequency, see equation (31).

9. Discussion

The goal of this article is to introduce the dFR into the context of PolInSAR. The reflectivity and data collection models presented by equations (44) and (47), respectively, are specifically

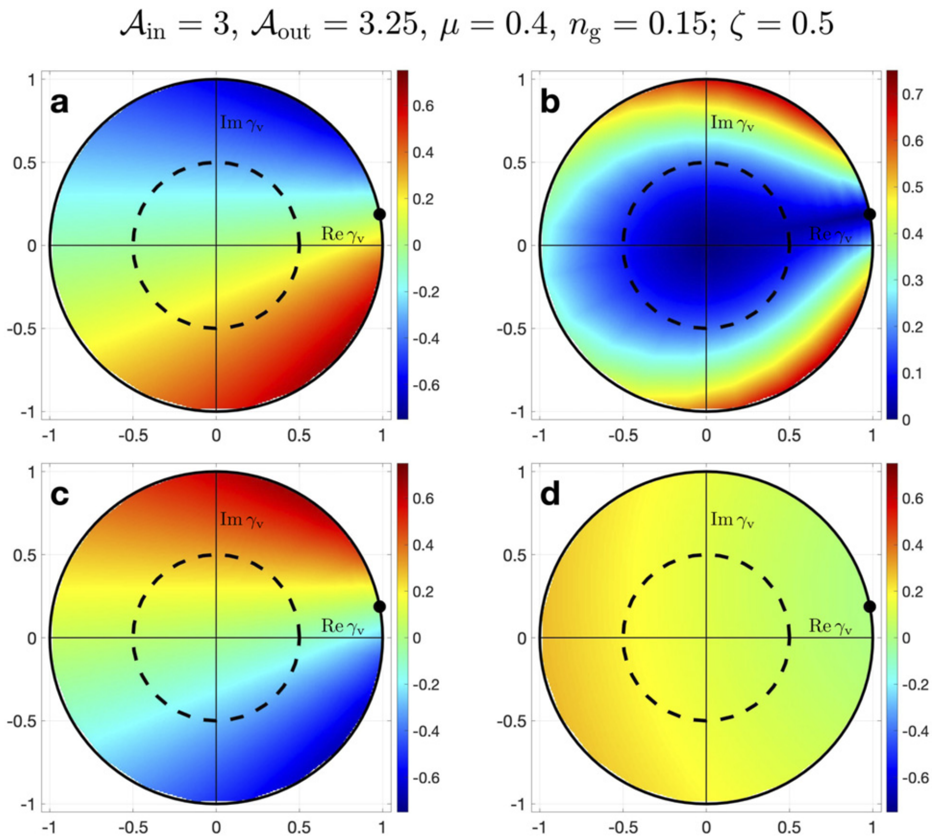

Figure 9. Same as in figure 6, but for $\mathcal{A}_{\rm out} \neq \mathcal{A}_{\rm in}$ as in section 9.

designed for this purpose. Although they exhibit many features of the standard RVoG model [42] that is used for reconstructing the properties of the vegetation layer from PolInSAR observations, they also are a result of multiple simplifications that may hamper the inversion if applied to real-life data.

For example, suppose that the dependence of foliage reflectivity on polarization that is characterized by the value of $\mathcal{A}$ in (44) is known only approximately rather than exactly. The effect of this uncertainty can be explored in the following scenario.

(a) Data are generated as in section 8.3, see (58), with $\mathcal{A} = \mathcal{A}_{\rm in}$.
(b) Inversion is performed according to (59)–(62), but with $\mathcal{A} = \mathcal{A}_{\rm out} \neq \mathcal{A}_{\rm in}$.

Figure 9 shows the resulting reconstruction errors for the case where the values of $\mathcal{A}_{\rm in}$ and $\mathcal{A}_{\rm out}$ differ by about 8%. The error magnitude is comparable to that in figure 6. Besides, the actual reflectivity measurements in SAR are subject to speckle [6], and the foliage layer itself is highly irregular, so achieving the accuracy of 10% or better for the parameter $\mathcal{A}$ cannot be guaranteed. A possible approach to correct this situation is to consider the value of $\mathcal{A}$ as unknown and increase the number of equations by including the measurements from additional polarizations. In this case, the reconstructed value of $\mathcal{A}$ will be specific to the particular location. However, this would make the analysis of the inversion more difficult.

We may also consider an alternative approach to evaluation of the effect of dFR on PolInSAR reconstruction, assuming a limited knowledge about dFR. As in the case of uncertainty in the value of $\mathcal{A}$, we can introduce an error in the value of q that controls the magnitude of dFR, see (54), at the reconstruction step of the following scenario.

(a) Data are generated using (47) and (49) with certain nonzero values of q and n_{g}. Hence, both dFR and noise are assumed present, see (54) and (57), as in section 8.4.

(b) Inversion is performed using the same formulation as for the data generation, but with a different value of the parameter that represents dFR, i.e., $q' \neq q$. The value of n'_{g} should be chosen to satisfy the condition that the reconstructed value of $\mathrm{e}^{\mathrm{i}\Psi'_Q}$ is on the unit circle on the complex plane (i.e., that Ψ'_Q is real). It is likely that $n'_{\mathrm{g}} \neq n_{\mathrm{g}}$.

While this scenario may look more realistic than that of section 8.4, it contains additional parameters, and each of its two steps is more complicated than before. We can expect that the results of simulation will be more difficult to characterize and interpret. Notwithstanding of that, this scenario is still based on the simplified system (47) that does not take into account one of the polarimetric channels and, for this reason, will need further generalization to be able to accommodate the real data.

Other venues of improvement for the model used in this work include:

- Taking into account the second co-polarized channel, VV, see (47) and table 1.
- In the current model, the only source of decorrelation outside the RVoG model (21) and (26) is the additive noise terms $\mathbf{N}^2$ in (47). However, in the case where the two images in the interferometric pair are acquired at different times, there is another important mechanism of decorrelation known as temporal decorrelation, which is due to the evolution of the scatterer between the two acquisition times. Obviously, changes of local weather and/or season affect the foliage scatterer by modifying its shape, density, water content, etc. Arguably, the ground scatterer may be considered less susceptible to variation under the same circumstances. The noise terms in model (47) will not capture this effect, whereas a more appropriate model describing this situation can be found in [59].

The main reason behind choosing the polarimetric model as simple as (47) is that it enables, for the first time, the evaluation of an entirely new physical effect, the dFR, in the context as complex as PolInSAR, see figure 1. In the original RVoG formulation, see (21) and (26), the PolInSAR system of equations presents a substantial challenge for inversion, requires additional considerations, and gives a limited analytic support for interpretation of the results of inversion [42]. Yet the RVoG model itself is also a simplification because it assumes (among other things) that the density of the scatterers in the vegetation layer is constant over the vertical coordinate, whereas the actual density functions are more complicated and depend on the forest type (see, e.g., [42, 57]). At the same time, the simplified systems (55) and (58) still possess the main characteristics of a polarimetric system in that they describe multiple channels, contain multiple types of scatterers, and use complex coherences as the data. Overall, the model we have chosen appears to strike a proper balance between the transparency, interpretability, and fidelity, and its results can be used as a benchmark for more comprehensive and sophisticated PolInSAR formulations.

10. Conclusions

For spaceborne Earth observation radars, dFR (section 6) introduces systematic errors into the ground topography, as well as the parameters of the vegetation layer (scattering volume above ground), reconstructed by PolInSAR. The magnitude of these errors depends on the characteristics of the radar system and the state of the Earth's ionosphere. Using a simplified polarimetric model, we have shown that for the existing X-, C-, and L-band spaceborne systems, these errors can be disregarded. For the contemplated P-band BIOMASS system, these errors are also small, but more borderline, see figures 7 and 8. However, for future systems that may combine even lower frequencies with high bandwidth, this result will need to be re-evaluated using a more comprehensive model, and approaches to mitigation of the dFR-induced errors should be introduced and analyzed. One possible approach to mitigation could involve the application of the PMF [23] that very substantially reduces the cross-channel contamination in plain polarimetric SAR imaging.

Acknowledgments

This work is supported by US AFOSR, Grants # FA9550-17-1-0230 and FA9550-21-1-0086.

Data availability statement

No new data were created or analysed in this study.

Appendix A. Linear chirps

SAR interrogating waveforms are linear frequency modulated pulses (chirps):

$$P(t) = A(t)\exp(-\mathrm{i}\omega_0 t),$$

where the slowly varying envelope is given by

$$A(t) = \chi_\tau(t)\exp(-\mathrm{i}\alpha t^2)$$

and the characteristic function χ_τ of the interval $[-\tau/2, \tau/2]$ is

$$\chi_\tau(t) = \begin{cases} 1, & t \in [-\tau/2, \tau/2], \\ 0, & \text{otherwise}. \end{cases}$$

The carrier frequency ω_0, bandwidth B, duration τ, and rate $\alpha > 0$ of the chirp are related by

$$2\alpha\tau = B \ll \omega_0 \quad \text{and} \quad B\tau \gg 1.$$

The instantaneous frequency of the chirp is obtained by differentiating $P(t)$ with respect to t inside the support of $A(t)$:

$$\omega(t) = \omega_0 + 2\alpha t = \omega_0 + \frac{B}{\tau}t, \quad |t| \leqslant \frac{\tau}{2}.$$

When the chirp $P(t)$ emitted by a point source at $\boldsymbol{x}$ propagates through the ionospheric plasma, its propagation becomes dispersive and not equivalent to pure retarded potentials:

$$P'(t, \boldsymbol{y}) = K(R_{\boldsymbol{y}})A'(t, \boldsymbol{y})\exp[-\mathrm{i}\omega_0(t - R_{\boldsymbol{y}}/v_{\mathrm{ph}})],$$

where $R_{\boldsymbol{y}} = |\boldsymbol{y} - \boldsymbol{x}|$, $K(R_{\boldsymbol{y}})$ accounts for the geometric decay in 3D, and

$$A'(t, \boldsymbol{y}) = \chi'_{\tau-\delta\tau}(t - R_{\boldsymbol{y}}/v_{\mathrm{gr}}) \exp[-\mathrm{i}(\alpha + \delta\alpha)(t - R_{\boldsymbol{y}}/v_{\mathrm{gr}})^2],$$

where

$$\delta\tau = \frac{B}{\omega_0}\frac{R_z}{c}\frac{\omega_{\mathrm{pe}}^2}{\omega_0^2} \quad \text{and} \quad \delta\alpha = \alpha\frac{\delta\tau}{\tau}.$$

The phase and group velocity are given by

$$v_{\mathrm{ph}} = \sqrt{\omega_{\mathrm{pe}}^2 + k^2c^2}/k \quad \text{and} \quad v_{\mathrm{gr}} = kc^2/\sqrt{\omega_{\mathrm{pe}}^2 + k^2c^2},$$

where for typical radar frequencies we have $\omega_{\mathrm{pe}}^2 \ll k^2c^2$.

Appendix B. Coherence on the complex plane

Consider a pair of random complex variables, a_1 and a_2, with $\langle |a_1|^2 \rangle = \langle |a_2|^2 \rangle = a^2$, where a is real. Take another such pair, b_1 and b_2, with $\langle |b_1|^2 \rangle = \langle |b_2|^2 \rangle = b^2$. The coherence within the pairs is defined by

$$\gamma_a = \frac{\langle \overline{a_1} a_2 \rangle}{\left(\langle |a_1|^2 \rangle \langle |a_2|^2 \rangle\right)^{1/2}} = \frac{\langle \overline{a_1} a_2 \rangle}{a^2}, \qquad \gamma_b = \frac{\langle \overline{b_1} b_2 \rangle}{\left(\langle |b_1|^2 \rangle \langle |b_2|^2 \rangle\right)^{1/2}} = \frac{\langle \overline{b_1} b_2 \rangle}{b^2}.$$

Suppose that there is no correlation between the pairs:

$$\langle \overline{a_1} b_1 \rangle = \langle \overline{a_1} b_2 \rangle = \langle \overline{a_2} b_1 \rangle = \langle \overline{a_2} b_2 \rangle = 0,$$

and consider the sums $c_1 = a_1 + b_1$ and $c_2 = a_2 + b_2$. The coherence between c_1 and c_2 will be given by

$$\gamma_c = \frac{\left\langle \overline{(a_1 + b_1)}(a_2 + b_2) \right\rangle}{\left(\langle |a_1 + b_1|^2 \rangle \langle |a_2 + b_2|^2 \rangle\right)^{1/2}} = \frac{\langle \overline{a_1} a_2 \rangle + \langle \overline{b_1} b_2 \rangle}{a^2 + b^2} = \gamma_a \frac{a^2}{a^2 + b^2} + \gamma_b \frac{b^2}{a^2 + b^2}. \tag{65}$$

Relation (65) shows that on the complex plane, γ_c is located on the segment of a straight line connecting the points γ_a and γ_b.

In the context of section 5, we can associate c_1 and c_2 with $\mathcal{I}(\boldsymbol{y}; \boldsymbol{x}^{(1)}, \ldots)$ and $\mathcal{I}(\boldsymbol{y}; \boldsymbol{x}^{(2)}, \ldots)$, respectively, see equations (8) and (22), a_1 and a_2 with the contributions to these images due to the ground, i.e., $\mathcal{I}_{\mathrm{Gr}}$, and b_1 and b_2 with the contributions due to the volume $\mathcal{I}_{\mathrm{Vol}}$. Accordingly, (65) with the help of (26) leads to (27).

Appendix C. Polarimetric radar interferometry with noise

Noise that affects the PolInSAR reconstruction may be due to the receiver, the evolution of the target when the two acquisitions are made at different times (temporal decorrelation), misregistration, etc [22]. To account for noise, we modify equation (22) as follows:

$$\begin{aligned} \mathcal{I}(\mathbf{w}; \boldsymbol{x}^{(1)}) &= \mathcal{I}_{\mathrm{Gr}}(\mathbf{w}; \boldsymbol{x}^{(1)}) + \mathcal{I}_{\mathrm{Vol}}(\mathbf{w}; \boldsymbol{x}^{(1)}) + N^{(1)}, \\ \mathcal{I}(\mathbf{w}; \boldsymbol{x}^{(2)}) &= \mathcal{I}_{\mathrm{Gr}}(\mathbf{w}; \boldsymbol{x}^{(2)}) + \mathcal{I}_{\mathrm{Vol}}(\mathbf{w}; \boldsymbol{x}^{(2)}) + N^{(2)}. \end{aligned} \tag{66}$$

The noise terms $N^{(1)}$ and $N^{(2)}$ in (66) are circular Gaussian, which is similar to the rest of the terms, and satisfy

$$\left\langle \overline{N^{(1)}} N^{(2)} \right\rangle = 0, \qquad \langle |N^{(1)}|^2 \rangle = \langle |N^{(2)}|^2 \rangle = \mathbf{N}^2,$$

where $\mathbf{N}^2$ is noise intensity. As a result, we have:

$$\gamma(\mathbf{w}) = \frac{V_Q \left(\sigma_{\mathrm{g}}^2(\mathbf{w})\gamma_{\mathrm{Gr}} + \sigma_{\mathrm{v}}^2(\mathbf{w})\gamma_{\mathrm{Vol}} \right)}{V_Q \left(\sigma_{\mathrm{g}}^2(\mathbf{w}) + \sigma_{\mathrm{v}}^2(\mathbf{w}) \right) + \mathbf{N}^2},$$

where V_Q is defined in (18). Then, we introduce the signal-to-noise ratio (SNR):

$$\mathrm{SNR}(\mathbf{w}) = \frac{V_Q \left(\sigma_{\mathrm{g}}^2(\mathbf{w}) + \sigma_{\mathrm{v}}^2(\mathbf{w}) \right)}{\mathbf{N}^2}$$

and rewrite the expression for $\gamma(\mathbf{w})$ in the form that resembles (27):

$$\gamma(\mathbf{w}) = \exp(\mathrm{i}\Psi_Q) \frac{\gamma_{\mathrm{v}} + m(\mathbf{w})}{1 + m(\mathbf{w})} \cdot \frac{\mathrm{SNR}(\mathbf{w})}{1 + \mathrm{SNR}(\mathbf{w})}.$$

For the special case $m(\mathbf{w}) = 0$, the previous formula reduces to

$$\gamma(\mathbf{w}) = \exp(\mathrm{i}\Psi_Q)\gamma_{\mathrm{v}} \cdot \frac{\mathrm{SNR}(\mathbf{w})}{1 + \mathrm{SNR}(\mathbf{w})}. \tag{67}$$

As the fraction on the right-hand side of (67) is real, $\gamma(\mathbf{w})$ lies on the segment of a straight line on the complex plane that connects the origin with $\exp(\mathrm{i}\Psi_Q)\gamma_{\mathrm{v}}$, as shown in figure 4.

ORCID iDs

Mikhail Gilman https://orcid.org/0000-0001-6970-627X

References

[1] Bamler R and Hartl P 1998 Synthetic aperture radar interferometry *Inverse Problems* **14** R1
[2] Rosen P A, Hensley S, Joughin I R, Li F K, Madsen S N, Rodriguez E and Goldstein R M 2000 Synthetic aperture radar interferometry *Proc. IEEE* **88** 333–82
[3] Cheney M and Borden B 2009 *Fundamentals of Radar Imaging* (*CBMS-NSF Regional Conference Series in Applied Mathematics*) vol 79 (Philadelphia, PA: SIAM)
[4] Jakowatz C V Jr, Wahl D E, Eichel P H, Ghiglia D C and Thompson P A 1996 *Spotlight-Mode Synthetic Aperture Radar: A Signal Processing Approach* (Dordrecht: Kluwer)
[5] Cumming I G and Wong F H 2005 *Digital Processing of Synthetic Aperture Radar Data. Algorithms and Implementation* (Boston, MA: Artech House Publishers)
[6] Oliver C and Quegan S 1998 *Understanding Synthetic Aperture Radar Images* (*Artech House Remote Sensing Library*) (Boston, MA: Artech House Publishers)
[7] Franceschetti G and Lanari R 1999 *Synthetic Aperture Radar Processing* (*Electronic Engineering Systems Series*) (Boca Raton, FL: CRC Press)
[8] Lee J-S and Pottier E 2009 *Polarimetric Radar Imaging from Basics to Applications* (*Optical Science and Engineering*) (Boca Raton, FL: CRC Press)
[9] Cheney M and Nolan C J 2004 Synthetic-aperture imaging through a dispersive layer *Inverse Problems* **20** 507–32
[10] Nolan C J and Cheney M 2004 Microlocal analysis of synthetic aperture radar imaging *J. Fourier Anal. Appl.* **10** 133–48

[11] Cheney M and Borden B 2005 Microlocal analysis of GTD-based SAR models *Algorithms for Synthetic Aperture Radar Imagery XII* (*International Society for Optics and Photonics, SPIE*) vol 5808 ed E G Zelnio and F D Garber pp 15–23
[12] Yarman C E, Yazici B and Cheney M 2007 Bistatic synthetic aperture radar imaging for arbitrary flight trajectories *IEEE Trans. Image Process.* **17** 84–93
[13] Gaburro R and Nolan C 2008 Microlocal analysis of synthetic aperture radar imaging in the presence of a vertical wall *J. Phys.: Conf. Ser.* **124** 012025
[14] Krishnan V P and Quinto E T 2011 Microlocal aspects of common offset synthetic aperture radar imaging *Inverse Problems Imaging* **5** 659–74
[15] Felea R and Nolan C 2015 Monostatic SAR with fold/cusp singularities *J. Fourier Anal. Appl.* **21** 799–821
[16] Farr T G *et al* 2007 The shuttle radar topography mission *Rev. Geophys.* **45** 1–33
[17] Krieger G, Moreira A, Fiedler H, Hajnsek I, Werner M, Younis M and Zink M 2007 TanDEM-X: a satellite formation for high-resolution SAR interferometry *IEEE Trans. Geosci. Remote Sens.* **45** 3317–41
[18] Gilman M and Tsynkov S 2022 A mathematical perspective on radar interferometry *Inverse Problems Imaging* **16** 119–52
[19] Reigber A and Moreira A 2000 First demonstration of airborne SAR tomography using multibaseline L-band data *IEEE Trans. Geosci. Remote Sens.* **38** 2142–52
[20] Cloude S R and Papathanassiou K P 1998 Polarimetric SAR interferometry *IEEE Trans. Geosci. Remote Sens.* **36** 1551–65
[21] Papathanassiou K P and Cloude S R 2001 Single-baseline polarimetric SAR interferometry *IEEE Trans. Geosci. Remote Sens.* **39** 2352–63
[22] Krieger G, Papathanassiou K P and Cloude S R 2005 Spaceborne polarimetric SAR interferometry: performance analysis and mission concepts *EURASIP J. Adv. Signal Process.* **2005** 354018
[23] Gilman M and Tsynkov S 2018 Differential Faraday rotation and polarimetric SAR. *SIAM J. Appl. Math.* **78** 1422–49
[24] Li L, Zhang Y, Dong Z and Liang D 2014 Ionospheric polarimetric dispersion effect on low-frequency spaceborne SAR imaging *IEEE Geosci. Remote Sensing Lett.* **11** 2163–7
[25] Le Toan T *et al* 2011 The BIOMASS mission: mapping global forest biomass to better understand the terrestrial carbon cycle *Remote Sens. Environ.* **115** 2850–60
[26] Heliere F, Fois F, Arcioni M, Bensi P, Fehringer M and Scipal K 2014 Biomass P-band SAR interferometric mission selected as 7th Earth explorer mission *EUSAR 2014; 10th European Conf. Synthetic Aperture Radar* (VDE) pp 1–4
[27] Wright P A, Quegan S, Wheadon N S and Hall C D 2003 Faraday rotation effects on L-band spaceborne SAR data *IEEE Trans. Geosci. Remote Sens.* **41** 2735–44
[28] Meyer F J and Nicoll J B 2008 Prediction, detection, and correction of Faraday rotation in full-polarimetric L-band SAR data *IEEE Trans. Geosci. Remote Sens.* **46** 3076–86
[29] Davies K and Smith E K 2002 Ionospheric effects on satellite land mobile systems *IEEE Antennas Propag. Mag.* **44** 24–31
[30] Pi X, Freeman A, Chapman B, Rosen P and Li Z 2011 Imaging ionospheric inhomogeneities using spaceborne synthetic aperture radar *J. Geophys. Res.* **116** 1–13
[31] Gail W B 1998 Effect of Faraday rotation on polarimetric SAR *IEEE Trans. Aerosp. Electron. Syst.* **34** 301–7
[32] Ishimaru A, Kuga Y, Liu J, Kim Y and Freeman T 1999 Ionospheric effects on synthetic aperture radar at 100 MHz to 2 GHz *Radio Sci.* **34** 257–68
[33] Meyer F J 2011 Performance requirements for ionospheric correction of low-frequency SAR data *IEEE Trans. Geosci. Remote Sens.* **49** 3694–702
[34] Jehle M, Frey O, Small D and Meier E 2010 Measurement of ionospheric TEC in spaceborne SAR data *IEEE Trans. Geosci. Remote Sens.* **48** 2460–8
[35] Gilman M and Tsynkov S 2018 Cross-channel contamination of PolSAR images due to frequency dependence of Faraday rotation angle *2018 IEEE Conf. Antenna Measurements Applications (CAMA)* (Västerås, Sweden) (Piscataway, NJ: IEEE) pp 1–4
[36] Li J, Ji Y, Zhang Y, Zhang Q and Dong Z 2018 Effects of ionosphere polarimetric dispersion on lower-frequency spaceborne SAR *2018 IEEE 3rd Int. Conf. Signal and Image Processing (ICSIP)* (Piscataway, NJ: IEEE) pp 510–5
[37] Smith E M and Tsynkov S V 2011 Dual carrier probing for spaceborne SAR imaging *SIAM J. Imaging Sci.* **4** 501–42

[38] Gilman M, Smith E and Tsynkov S 2013 Reduction of ionospheric distortions for spaceborne synthetic aperture radar with the help of image registration *Inverse Problems* **29** 054005
[39] Gilman M, Smith E and Tsynkov S 2017 Transionospheric synthetic aperture imaging *Applied and Numerical Harmonic Analysis* (Basel: Birkhäuser)
[40] Gilman M and Tsynkov S 2015 A mathematical model for SAR imaging beyond the first Born approximation *SIAM J. Imaging Sci.* **8** 186–225
[41] Zitová B and Flusser J 2003 Image registration methods: a survey *Image Vis. Comput.* **21** 977–1000
[42] Cloude S 2010 *Polarisation: Applications in Remote Sensing* (Oxford: Oxford University Press)
[43] Zebker H A and Villasenor J 1992 Decorrelation in interferometric radar echoes *IEEE Trans. Geosci. Remote Sens.* **30** 950–9
[44] Moreira A, Prats-Iraola P, Younis M, Krieger G, Hajnsek I and Papathanassiou K P 2013 A tutorial on synthetic aperture radar *IEEE Geosci. Remote Sens. Mag.* **1** 6–43
[45] Hanssen R F 2001 *Radar Interferometry: Data Interpretation and Error Analysis* (*Remote Sensing and Digital Image Processing*) vol 2 (Dordrecht: Kluwer)
[46] Massonnet D and Souyris J-C 2008 *Imaging with Synthetic Aperture Radar* (*Engineering Sciences: Electrical Engineering*) (Lausanne: EFPL Press) Distributed by CRC Press
[47] Cloude S R and Papathanassiou K P 2003 Three-stage inversion process for polarimetric SAR interferometry *IEE Proc. Radar Sonar Navig.* **150** 125–34
[48] Ulaby F T and Elachi C 1990 *Radar Polarimetry for Geoscience Applications* (*The Artech House Remote Sensing Library*) (Boston, MA: Artech House Publishers)
[49] Born M and Wolf E 1999 *Principles of Optics: Electromagnetic Theory of Propagation, Interference and Diffraction of Light* Seventh (expanded) edn With contributions by ed A B Bhatia, P C Clemmow, D Gabor, A R Stokes, A M Taylor, P A Wayman and W L Wilcock (Cambridge: Cambridge University Press)
[50] Stratton J A 1941 *Electromagnetic Theory* (New York: McGraw-Hill)
[51] Ginzburg V L 1964 *The Propagation of Electromagnetic Waves in Plasmas* (*International Series of Monographs on Electromagnetic Waves*) vol 7 (Oxford: Pergamon)
[52] Landau L D and Lifshitz E M 1984 *Electrodynamics of Continuous Media* (*Pergamon International Library of Science, Technology, Engineering and Social Studies, Course of Theoretical Physics*) vol 8 (Oxford: Pergamon) Translated from the second Russian edition by J B Sykes, J S Bell and M J Kearsley, second Russian edition revised by Lifshits and L P Pitaevskii
[53] Swanson D G 2003 *Plasma Waves* (*Series in Plasma Physics and Fluid Dynamics*) 2nd edn (Bristol: Institute of Physics Publishing)
[54] Gilman M, Smith E and Tsynkov S 2014 Single-polarization SAR imaging in the presence of Faraday rotation *Inverse Problems* **30** 075002
[55] Voronovich A 1999 *Wave Scattering from Rough Surfaces* (Berlin: Springer)
[56] Kasilingam D, Schuler D and Lee J-S 2001 The depolarization of radar backscatter from rough surfaces due to surface roughness and slopes *IGARSS 2001. Scanning the Present and Resolving the Future. Proc. IEEE 2001 Int. Geoscience and Remote Sensing Symposium (Cat. No. 01CH37217)* vol 2 (Piscataway, NJ: IEEE) pp 925–7
[57] Brigot G, Simard M, Colin-Koeniguer E and Boulch A 2019 Retrieval of forest vertical structure from PolInSAR data by machine learning using LIDAR-derived features *Remote Sens.* **11** 381
[58] Kankaku Y, Suzuki S and Osawa Y 2013 ALOS-2 mission and development status *2013 IEEE Int. Geoscience and Remote Sensing Symp.-IGARSS* (Piscataway, NJ: IEEE) pp 2396–9
[59] Papathanassiou K P and Cloude S R 2003 The effect of temporal decorrelation on the inversion of forest parameters from Pol-InSAR data *Int. Geoscience and Remote Sensing Symp.* vol 3 pp 1429–31